Ph.D. Dissertation of Feiyan Zhu

Efficient Multiscale Homogenization Model for Sheet Molding Compound (SMC) with Random Wavy Fibers and Overlapping Structures

무작위 물결 섬유와 겹치는 구조를 가진 SMC (Sheet Molding Compound)를 위한 효율적인 멀티 스케일 균질화 모델

August 2023

Graduate School of Engineering
Seoul National University
Aerospace Engineering Major

Feiyan Zhu

Efficient Multiscale Homogenization Model for Sheet Molding Compound (SMC) with Random Wavy Fibers and Overlapping Structures

Feiyan Zhu

Submitting a Ph.D. Dissertation of
Engineering
August 2023

Graduate School of Engineering
Seoul National University
Aerospace Engineering Major

Feiyan Zhu

Confirming the Ph.D. Dissertation written by
Feiyan Zhu
August 2023

Chair _____(Seal)
Vice Chair _____(Seal)
Examiner _____(Seal)
Examiner _____(Seal)
Examiner _____(Seal)

Abstract

Multiscale finite element analysis (FEA) has proven to be an effective method in modeling the behavior of composite materials. However, their practical applicability is limited due to the high computational cost associated with multiscale models. This thesis proposes a multiscale clustering-based self-consistent analysis (SCA) for composite materials, which aims to reduce computation time without sacrificing accuracy. The proposed approach addresses the need for efficient modeling of SMC composites and the challenges of applying a multiscale homogenization model to real-world applications.

An improved analytical homogenization model and a clustering-based SCA model are presented and compared for the efficient modeling of SMC composites. Due to the complex structure of SMC, traditional homogenization models face challenges in accurately capturing its behavior. The improved analytical homogenization model incorporates the Mori-Tanaka method, considering factors such as wavy fiber, ductile damage, SMC chip orientation, and overlap of SMC chips. On the other hand, the clustering-based SCA model is a numerical multiscale model that considers randomly wavy fibers and randomly oriented SMC chips while maintaining computational efficiency. Both homogenization models are thoroughly validated and demonstrate their effectiveness and accuracy in capturing the behavior of SMC composites. The comparison between the presented SCA model and traditional multiscale FEA models highlights the significant reduction in computation time achieved while maintaining accuracy and validity. The influences of various geometric features of fibers and SMC chips are demonstrated in predicting the mechanical properties of composites.

Keywords: Composites, multiscale model, FEA, self-consistent analysis

Student Number: 2019-38802

Table of Contents

List of Figures

List of Tables

Chapter 1. Introduction

1.1. Study Background

Carbon nanotubes (CNTs) have gained immense popularity in the 21st century due to their exceptional mechanical properties. With Young's modulus of 1TPa, tensile strength 20 times that of high-strength steel alloys, and thermal conductivity of almost double that of pure diamond[1], CNTs have become one of the most sought-after materials for various applications. Since their discovery in 1991 by Iijima[2], there has been enormous research on CNT nano-fillers from different perspectives[3-7]. CNTs are an excellent reinforcing filler for polymeric matrix composites, and their properties are influenced by various factors such as waviness, dispersion, fiber orientation, bonding conditions, and interphase materials between the CNT fibers and matrix. All these factors significantly impact the mechanical and electrical properties of CNT-reinforced polymeric nanocomposite materials.

Various models have been proposed to simulate the effective properties of CNT nanocomposites[8, 9]. However, the effects of inner fiber and matrix properties, waviness, interfacial debonding, and dispersions of CNTs have rendered disputes on comparisons between experimental data and theoretical predictions[10]. Therefore, modeling efforts have focused on those geometric features of CNTs, which are complicated by various factors. For instance, Hammerand et al.[11] reported that the effects of the interphase regions on the effective properties are more significant than the clustering effects, while Fisher et al.[12] reported that the waviness and orientations can also reduce the effective stiffness. Several researchers have proposed prediction methods for aligned or randomly oriented composite properties linked with the dispersion of fibers in CNT nanocomposites via finite elements and Mori-Tanaka micromechanics theory[13-17].

While linear damage models for CNT nanocomposites that simulate elastic conditions have been studied, nonlinear plasticity models attract more attention. In this regard, there has been significant research on the behavior of fiber composites, and several plastic damage models have been proposed. This thesis focuses on modeling the elasto-plastic behavior of CNT nanocomposites with interfacial damage and ductile damage in the matrix phase since the damage is an inevitable element in simulations. Specifically, an improved method is introduced to simulate CNT nanocomposites in the elastic range and consider the situation where plasticity occurs. The strain-stress curve is nonlinear when plasticity occurs, and plastic effective properties are related to the hardening function, plastic strain, and ductile damage. Hence, elasto-plastic properties have always been one of the most exciting properties of composites. A nonlinear composite model is proposed in the plastic range using the Mori-Tanaka method with interfacial damage, and ductile damage is introduced by using the Lemaitre-Chaboche damage modeling method.

Additionally, since the effective properties difference between the matrix and inclusion is usually significant, assuming the inclusion is always elastic during the simulation while the matrix will become plastic with increasing strain. On the other hand, multiscale transformation is proposed to achieve macro stress and strain increment. Moreover, there are few studies on the stochastic modeling of CNT nanocomposites. Hence, a model for stochastically aligned wavy CNTs is introduced. This thesis contributes to developing a comprehensive and accurate model for predicting the mechanical properties of CNT nanocomposites.

Fiber-reinforced composites (FRC) are composite materials made of a matrix material reinforced with fibers. These fibers can be made from various materials, such as glass, carbon, or aramid, and are embedded within the matrix to enhance its mechanical properties[18-20]. FRC materials are extensively used in various aerospace, automotive, and construction industries due to their desirable properties, such as high strength-to-weight ratio, corrosion resistance, durability, and customization options[21, 22].

FRC materials offer superior mechanical and physical properties to conventional materials such as metals and polymers, making them ideal for structural applications. Combining high-strength fibers and matrix materials results in composite materials that can withstand high loads, impact forces, and extreme temperatures. FRC materials are widely used in applications that require lightweight and strong materials, such as aircraft and spacecraft components.

Sheet Moulding Composites (SMC) is a fiber-reinforced composite material that has gained popularity due to its versatility, durability, and cost-effectiveness[23-25]. SMCs are created by combining chopped fibers, thermosetting resins, and additives into a mold and then applying heat and pressure to fuse the components. The result is a lightweight, high-strength material ideal for various applications across several industries[26-28].

The mechanical properties of SMC composites are affected by various parameters such as fiber orientation, fiber volume fraction, and matrix properties[29]. The final molded parts of SMC show uneven distributions of fiber chips due to the complex flow pattern during the compression molding process. It leads to significant inhomogeneity and anisotropy in the composite material, which poses a challenge while predicting the behavior of SMC composites in virtual tests[30]. Numerous studies have been reported to deal with the heterogeneity of SMC composites using analytical or computational micromechanics models. Both micromechanics models for SMC composites have been developed to estimate the effective properties of micro/mesostructured by constructing a representative volume element (RVE)[31-33].

The RVE is constructed using the finite element (FE) method as a computational micromechanics model. Jiang et al.[34] presented the FE-based RVE model with a single short fiber and discussed the effects of fiber orientation and aspect ratio on the mechanical properties of composites. Based on the short-fiber modeling, Li et al.[35] developed a finite element SMC model with the random fiber orientation. The rotational transformation calculated the rotated stiffness tensors of short fibers and assigned them to the SMC FE RVE model.

Next, Chen et al.[36] presented a more realistic SMC model through a stochastic reconstruction algorithm to express the undulation of overlapping between fiber chips. The modified random sequential adsorption (RSA) was adopted to the reconstruction algorithm and generated each SMC layer to deal with the overlapped parts. Recently, Sun et al.[37] developed a woven RVE with a finite element method to cope with the overlapping portions of SMC.

Multiscale simulation is adopted to deal with complicated structural fiber-reinforced composites. Multiscale simulation is a rapidly developing field that has been adopted to deal with complex structural fiber-reinforced composites. In recent years, these composites have been used widely in numerous applications, including aerospace, automotive and civil engineering. An approach to quantifying the uncertainty of composites due to geometric variation is proposed[38]. A concurrent SCA2 framework from microscale to mesoscale is established to capture the non-linear behavior of 3D braided composites[39]. The application of multiscale simulation has proven to be a practical approach to predicting the mechanical properties of these materials and gaining a better understanding of their underlying microstructures.

Multiscale simulation has a wide range of applications in fiber-reinforced composites. One of the main applications is predicting the mechanical properties of these nano- and micro- composites[40]. By modeling the microstructure of the composite, researchers can accurately predict various spatial uncertainties[41].

On the other hand, the clustering-based method is widely applied in the computational model. K Popat et al. provide a cluster-based probability model and uses it to image and texture processing [42]. Clustering-based anomaly detection in multivariate time series data is proposed by Jinbo Li[43].

The multiscale simulation approach for SMC can be broadly categorized into two main methodologies: computational and analytical methods. These methods are continually evolving with ongoing efforts to enhance their effectiveness in modeling the complex structures inherent in SMC materials. The computational method yields

relatively accurate results, albeit at the expense of extensive computational resources due to the large number of calculations involved. Consequently, there is a pressing need to prioritize the improvement of computation speed, thereby enabling more efficient simulations without compromising accuracy.

1.2. Purpose of Research & Thesis Overview

This study aims to investigate the effects of random chip orientation and overlapping SMC chips on the formation of complex structures. Additionally, this research aims to compare the mechanical performance, formability, and manufacturing of SMC composites with traditional continuous fiber composites. Furthermore, this study explores the limitations of computational and analytical models in simulating SMC composites. This research aims to provide valuable insights into developing and optimizing SMC composites for use in complex geometrical structures, such as landing gears or chassis parts.

Moreover, this research investigates the limitations of current macroscale models in analyzing micromechanical damage and detailed structures. The study will also explore the potential benefits of multiscale simulations in improving the accuracy and reducing costs of such analyses. Through an in-depth review of the literature and analysis of case studies, this research aims to highlight the need for multiscale simulation approaches in addressing the challenges of analyzing complex material behavior and damage mechanisms. The findings of this study are expected to contribute to the advancement of materials engineering and structural analysis by providing insights for developing more accurate and efficient simulation techniques.

This research paper aims to investigate the homogenization methodology and multiscale analysis of composite materials. Composite materials are widely used in various industries due to their unique properties, but their complex structures make it challenging

to predict their behavior accurately. Homogenization methods can help simplify the analysis of complex systems by providing adequate ways to determine their macroscopic properties.

The thesis is working on the geometric modeling of inclusions (i.e., random waviness and orientation) and elastic-plastic, ductile damage simulation in the micromechanics composites model, combining the micromechanics model with clustering-based self-consistent analysis to establish a multiscale composites model and apply the model on SMC. Based on the complicated structure of SMC, random chip orientation and random waviness are adopted to design a more realistic multiscale model.

The thesis introduces a novel approach incorporating geometric modeling of inclusions and elastic-plastic, ductile damage simulation in micromechanics composites models. The proposed model considers random waviness and inclusions' orientation, a more realistic representation of composite materials. The novelty of this work lies in the combination of this micromechanics model with clustering-based self-consistent analysis, which enables the establishment of a multiscale composites model. The model is then applied to study sheet molding compound (SMC), which has a complicated structure with random chip orientation and waviness. This approach provides a better understanding of the mechanical behavior of SMC and can lead to the development of more optimized composite materials. A hierarchical multistep homogenization model of SMC is also represented. It is a numerical model based on Mori-Tanaka homogenization considering the overlapping structures of SMC. The comparison of two homogenization models presents the validity and feasibility of the modeling of SMC composites. Overall, this thesis contributes to advancing the field of composites modeling and has practical implications for the design and optimization of composite materials.

Chapter 1 serves as an introduction, providing a comprehensive background, emphasizing the inherent complexity of composite materials and the challenges involved in predicting their behavior. The chapter highlights the significance of homogenization methods and multiscale analysis in addressing these challenges.

Moving on to Chapter 2, the analytical and numerical homogenization methods are introduced, specifically focusing on the cluster-based Lippmann-Schwinger and Mori-Tanaka homogenization methods. These two widely used approaches have demonstrated their effectiveness in analyzing composite materials.

In Chapter 3, the clustering-based analysis of offline databases is presented. The chapter outlines the essential steps involved in domain decomposition and the determination of interaction tensors, which form the foundation for offline analysis of clustering data. This technique plays a crucial role in accurately predicting the material properties. Additionally, the chapter delves into the clustering-based analysis of online self-consistent analysis, aiming to provide a real-time approach for predicting the behavior of composite materials under dynamic conditions.

Additionaly, an improved linear and nonlinear Mori-Tanaka homogenization model, offering enhanced capabilities for simulating the behavior of composites. Building upon this, compares the models presented in Chapter 3, providing insights into their relative strengths and limitations.

Shifting the focus to SMC composites, Chapter 4 presents the multistep homogenization method. This chapter outlines the procedures for domain decomposition and introduces a hierarchical structure for the multistep homogenization approach, which proves instrumental in accurately characterizing SMC composites.

Also, Chapter 4 discusses multiscale self-consistent analysis (SCA) composite materials simulation techniques, specifically focusing on the offline database and online calculation methods introduced in Chapter 3. These techniques offer valuable insights into the behavior of composites at different length scales.

Chapters 5 delves into the results of the improved Mori-Tanaka model and the multiscale clustering-based SCA model, respectively. These chapters present and analyze the findings, contributing to a deeper understanding of composite materials.

Finally, Chapter 6 concludes the thesis, summarizing the essential findings and their implications. The thesis presents a novel

approach to composite modeling by incorporating geometric modeling of inclusions and elastic-plastic, ductile damage simulation in micromechanics models. The contributions of this study have practical implications for the design and optimization of composite materials, advancing the field of composites modeling and analysis. This model includes random waviness and orientation of inclusions, which provides a more realistic representation of composite materials. The proposed approach combines this micromechanics model with clustering-based self-consistent analysis to establish a multiscale composites model. The model is applied to study sheet molding compound (SMC), a complex material with random chip orientation and waviness. The study provides a better understanding of the mechanical behavior of SMC and can lead to the development of more optimized composite materials.

Furthermore, this thesis presents a hierarchical multistep homogenization model of SMC based on Mori-Tanaka homogenization, which considers the overlapping structures of SMC. The comparison of two homogenization models demonstrates the validity and feasibility of the modeling of SMC composites. This work contributes to advancing the field of composites modeling and has practical implications for the design and optimization of composite materials. It provides a better understanding of the behavior of SMC and presents a novel approach to multiscale composite modeling.

Chapter 2. Homogenization Methodology

As a part of this thesis, the focus is on simulating carbon nanotube (CNT) nanocomposites, which are typical fiber inclusion composites. To achieve this, most homogenization methods can be applied. Chamis proposed a simplified micromechanics model (SMM) with the rule of mixture (ROM), which is based on the material properties of the inclusion and matrix. This approach has been widely used to predict the elastic properties of various composite materials under different boundary conditions [44-48]. The Halpin and Tsai model is one of the most commonly used micromechanics models for predicting elastic properties in fiber composites. The Halpin-Tsai Equation[49], based on Hill's self-consistent micromechanics method, was first proposed by Halpin and Tsai in 1976 and has since been widely used in CNT composite modeling [50, 51].

To further improve the accuracy of the model, Hopkins and Chamis[52, 53] developed a refined model for shear and transverse properties by using simple relations among fiber size and volume fraction. This advanced model has been applied in many fiber-like inclusion composites [54] and can be helpful in accurately predicting the mechanical behavior of CNT nanocomposites. Overall, this work aims to advance the field of composites modeling, specifically in the context of CNT nanocomposites.

In computational micromechanics, the finite element model has emerged as the most widely utilized approach due to its high accuracy in handling complex fiber packing configurations. One of the pioneering works in this area was carried out by Caruso and Chamis[53], who developed a single-cell finite element model in 1986. This model served as a foundation for subsequent advancements in the field. Building upon this, Finegan and Gibson presented examples of 2D and 3D finite element quarter domain

models[55], further expanding the capabilities of finite element modeling in composite materials.

Since then, there has been a growing adoption of finite element models for simulating carbon nanotube (CNT) nanocomposites at the microscale. Numerous researchers have employed finite element models to investigate the mechanical behavior and properties of CNT nanocomposites[56, 57]. These models offer the advantage of capturing the intricate details of the microstructure and enable a comprehensive analysis of the effects of various factors, such as fiber arrangement and interface interactions, on the overall behavior of the composite.

The utilization of finite element models in CNT nanocomposite simulation has dramatically contributed to advancing the understanding of the mechanical response of these materials. By incorporating the complex microstructure and material properties into the finite element framework, researchers have been able to accurately predict and analyze the behavior of CNT nanocomposites under different loading conditions.

2.1. Lippmann Schwinger Homogenization

Lippmann-Schwinger homogenization is a mathematical technique used to model and study the behavior of composite materials[58]. It provides a framework for analyzing the effective properties of materials made up of multiple components with different physical properties, such as fiber-reinforced composites.

The Lippmann-Schwinger homogenization approach has been used extensively in the study of composite materials and has been successfully applied to various systems, including photonic crystals, metamaterials, and natural composites such as wood.

The Lippmann-Schwinger equation, which forms the basis of this homogenization method, is derived from the theory of scattering in quantum mechanics. It is an integral equation that relates the total field to the incident field and the scattered field, considering the interactions between the scattering objects. In the context of homogenization, the Lippmann-Schwinger equation is adapted to describe the interactions between the constituent phases of a composite material.

By solving the Lippmann-Schwinger equation, one can obtain the effective properties of the composite material, such as the effective conductivity, elastic modulus, or thermal conductivity. This method is advantageous when dealing with composites that exhibit complex microstructures or contain highly contrasting material phases.

The Lippmann-Schwinger homogenization method, originally proposed by Moulinec and Suquet [59], provides a practical approach for solving the corrector problem in heterogeneous materials. This method involves reformulating the corrector problem as an integral equation, commonly known as the Lippmann-Schwinger equation. Discretizing this equation on a regular grid makes it amenable to computational analysis.

Since its original introduction, the Lippmann-Schwinger method has undergone further developments and refinements, resulting in several variants of the basic scheme. Researchers have proposed modifications and extensions to address specific challenges and incorporate additional features. Brisard and Dormieux propose a new formulation as a Galerkin discretization of the Lippmann-Schwinger Equation[60]. Matti Schneider[61] improves the Lippmann-Schwinger equation solvers for the computational homogenization of materials with pores. The work by Ma et al. showcases the capability of FFT-based homogenization techniques in analyzing the hypoelastic-plastic behavior of materials subjected to finite strains.

[62]. These variants aim to improve accuracy, handle more complex material microstructures, or address specific physical phenomena.

Over the years, the Lippmann-Schwinger method has found wide application across various disciplines, including materials science, mechanics, and electromagnetics[63-67]. Its ability to efficiently handle periodic boundary conditions and discretize integral equations has made it particularly attractive for researchers seeking to study and understand the behavior of complex heterogeneous systems.

Firstly, the local stress is supposed to be divided into two parts: the reference stress and polarization stress, as shown in Equation (1).

$$\boldsymbol{\sigma}(\boldsymbol{x}) = \boldsymbol{C}^0 : \boldsymbol{\varepsilon} + \boldsymbol{p}(\boldsymbol{x}) \tag{1}$$

Where $\boldsymbol{C}^0$ is reference elastic modulus and $\boldsymbol{p}$ is polarization stress. Green's function is introduced to obtain the integral equation[68].

$$\boldsymbol{\varepsilon}(\boldsymbol{x}) + \int_{\Omega} \Phi^0(x, x') : \boldsymbol{p}(\boldsymbol{x}) dx' - \boldsymbol{\varepsilon}^0 = 0 \tag{2}$$

Where $\boldsymbol{\varepsilon}^0$ is far-field strain and it is homogenous in the reference material. Substitute Equation (1) into (2) and get.

$$\boldsymbol{\varepsilon}(\boldsymbol{x}) + \int_{\Omega} \Phi^0(x, x') : (\boldsymbol{C}^0 : \boldsymbol{\varepsilon}(\boldsymbol{x}') - \boldsymbol{\sigma}(\boldsymbol{x}')) dx' - \boldsymbol{\varepsilon}^0 = 0 \tag{3}$$

Equation (3) is known as Lippmann Schwinger Equation and can also be expressed as incremental form.

$$\Delta\boldsymbol{\varepsilon}(\boldsymbol{x}) + \int_{\Omega} \Phi^0(\boldsymbol{x}, \boldsymbol{x}') : (\boldsymbol{C}^0 : \Delta\boldsymbol{\varepsilon}(\boldsymbol{x}') - \Delta\boldsymbol{\sigma}(\boldsymbol{x}')) dx' - \Delta\boldsymbol{\varepsilon}^0 = 0 \tag{4}$$

When conducting simulations of the mechanical properties of entire composite materials' Representative Volume Elements (RVE), using Lippmann Schwinger's equation for each point can be a time-consuming process. Therefore, an alternative method based on clustering has been developed as an improved approach.

2.2. Cluster-based LS Homogenization

The cluster-based Lippmann-Schwinger homogenization approach is improved Lippmann-Schwinger homogenization to reduce calculation time. Instead of being based on an element of each RVE, RVE divided by clusters provides an efficient and accurate way to simulate the composite material.

Now suppose the RVE of composites is composed by N cluster, the characteristic function is.

$$\boldsymbol{\chi^I} = \begin{cases} 1 & if\ x \in \Omega^I \\ 0 & otherwise \end{cases} \tag{5}$$

Where $I = 1 \ldots N$ represents the number of clusters, and Ω^I indicates the domain of certain cluster. Therefore, the Lippmann Schwinger Equation as shown in Equation (4) is become.

$$\frac{1}{c^I|\Omega|}\int_{\Omega} \boldsymbol{\chi^I}(\boldsymbol{x})\,\Delta\boldsymbol{\varepsilon}(\boldsymbol{x})d\boldsymbol{x} +$$

$$\frac{1}{c^I|\Omega|}\int_{\Omega}\int_{\Omega} \boldsymbol{\chi^I}(\boldsymbol{x})\boldsymbol{\Phi}^0(\boldsymbol{x},\boldsymbol{x}'):(\boldsymbol{C}^0:\Delta\boldsymbol{\varepsilon}(\boldsymbol{x}') - \Delta\boldsymbol{\sigma}(\boldsymbol{x}'))d\boldsymbol{x}'d\boldsymbol{x} - \Delta\boldsymbol{\varepsilon}^0 = 0 \tag{6}$$

Where c^I is volume fraction of I-th cluster, and the interaction tensor[69] between two clusters is defined by.

$$\boldsymbol{D^{IJ}} = \frac{1}{c^I|\Omega|}\int_{\Omega}\int \boldsymbol{\chi^I}(\boldsymbol{x})\boldsymbol{\chi^J}(\boldsymbol{x})\boldsymbol{\Phi}^0(\boldsymbol{x},\boldsymbol{x}')d\boldsymbol{x}'d\boldsymbol{x} \tag{7}$$

So, Equation (6) can be expressed as.

$$\Delta\boldsymbol{\varepsilon}^I + \sum_{I=1}^{k}\boldsymbol{D}^{IJ}:[\Delta\boldsymbol{\sigma}^J - \boldsymbol{C}^0:\Delta\boldsymbol{\varepsilon}^J] - \Delta\boldsymbol{\varepsilon}^0 = 0 \tag{8}$$

To solve the integral equation, boundary condition is considered. Macroscopic strain and stress boundary condition is calculated by.

$$\Delta\bar{\boldsymbol{\varepsilon}} = \sum_{I=1}^{k} c^I\,\Delta\boldsymbol{\varepsilon}^I \tag{9}$$

$$\Delta\bar{\boldsymbol{\sigma}} = \sum_{I=1}^{k} c^I\,\Delta\boldsymbol{\sigma}^I \tag{10}$$

To improve calculation time, the multiscale model can be for clustering-based Lippmann Schwinger divided into online and offline processes.

The online analysis primarily involves the iteration for strain increment step and the update reference material constitutive matrix. This process occurs during the actual simulation and serves to enhance the accuracy of the model's predictions.

On the other hand, the offline process focuses on saving the database for calculating the interaction tensor between clusters and loading cluster position distributions. This helps to reduce computational overhead and further improves the efficiency of the model.

It is essential to note that both the online and offline processes are critical for the success of the multiscale model for clustering-based Lippmann Schwinger. When used together, they allow for accurate and efficient simulations that can be applied to a wide range of real-world scenarios.

The offline and online processes will be introduced in Section 2.2.1 and 2.2.3 respectively.

2.2.1 Domain Decomposition

In this section, a k-means method provides an effective way of identifying points in the material with similar behavior and can be used alongside other characterization techniques to gain a comprehensive understanding of the material[70].

The strain concentration tensor A(x) can be used to identify points in the material with similar mechanical behavior. Similar strain concentrations indicate that the material is responding in a similar way to stress and strain and may therefore require a similar design approach.

As shown in Equation (30), strain concentration tensor is related to elastic microscale strain and macroscale strain.

In order to utilize this data to study and predict the mechanical behavior of these materials, it is necessary to first establish a similarity metric between different material points based on their strain concentration tensors. As mentioned earlier, equivalent tensors indicate equivalent mechanical behavior and should be clustered accordingly. One potential approach is to use a clustering algorithm such as k-means clustering method.

Once the material points have been clustered based on their strain concentration tensors, their nonlinear plastic response can be studied. The localization of plasticity, which is the process by which plastic deformation becomes concentrated in certain regions of the material, is known to occur at points with high strain concentrations. Therefore, points within the same cluster should have similar plastic response and failure modes under loading.

It is worth noting that the format of the raw data for 3D materials will be more complex, due to the increased number of independent components for the strain concentration tensor. However, the overall

approach for studying the similarity and mechanical behavior of these materials remains the same. With the availability of high-fidelity DNS simulations and advanced data analysis techniques, it is now possible to gain deeper insights into these materials and accelerate their development for various applications.

K-means is a clustering algorithm used to group data points into K clusters based on their similarity. The algorithm works by iteratively assigning data points to the nearest cluster center, also known as the centroid, and updating the centroid based on the new cluster members.

Suppose the strain concentration tensor of each element is given, and then.

$$S = argmin \sum_{J=1}^{N} \sum_{m \in S^J} \|\boldsymbol{A}^m - \bar{\boldsymbol{A}}^J\|^2 \qquad (11)$$

Where $\boldsymbol{A}^m$ and $\bar{\boldsymbol{A}}^J$ are strain concentration tensor for m-th point and mean strain concentration tensor in J-th cluster. The k-means method is.

1. Choose the number of clusters N that you want to create.
2. Initialize k $\boldsymbol{A}^k$ randomly (where k=1...N).
3. Assign each data point to the nearest $\boldsymbol{A}^k$.
4. Recalculate the $\boldsymbol{A}^k$of each cluster based on the new cluster members.
5. Repeat steps 3 and 4 until find the minimum $\boldsymbol{A}^k$ as shown in Equation (11).

The goal of the algorithm is to minimize the sum of squared distances between each data point and its assigned $\boldsymbol{A}^k$. K-means is a widely used algorithm for clustering because it is relatively fast and easy to understand.

Periodic boundary conditions are commonly used in simulations of periodic systems, such as lattices or crystal structures. These conditions require the displacement or deformation of each boundary point to be the same as the corresponding point on the opposite boundary. Essentially, this means that the boundaries of the system are identified with one another, and the system is assumed to repeat indefinitely in all directions. Periodic boundary conditions are used to simulate large-scale systems and are commonly employed in fiber-reinforced composites material.

Periodic boundary condition is adopted to get strain concentration tensor for each Gauss point in finite element model in ABAQUS.

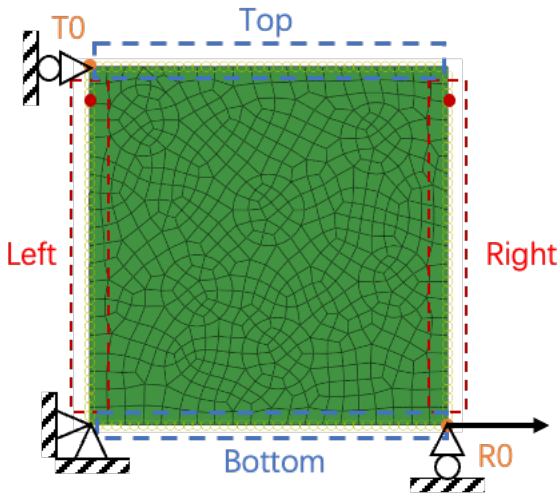

Figure 1. Periodic boundary condition application in ABAQUS

Figure 1 indicates the periodic boundary condition applied in FE model in ABAQUS and following.

$$\begin{aligned} u^R - u^L - u^{R0} &= 0 \\ v^R - v^L &= 0 \\ v^T - v^B - v^{T0} &= 0 \\ u^T - u^B &= 0 \end{aligned} \tag{12}$$

Equation (12) shows requirement of replicating an equal and opposite displacement across the boundary.

2.2.2 Interaction tensor

A key advantage of the Lippmann-Schwinger method is its efficient implementation using the fast Fourier transform (FFT) algorithm. This enables the convolution product appearing in the Lippmann-Schwinger equation, subject to periodic boundary conditions, to be computed rapidly. The FFT-based approach significantly enhances the computational efficiency of the method, making it well-suited for practical applications.

Interaction tensor describes the interaction between clusters due to the irregular shape of each cluster. Interaction tensor is defined as

$$\boldsymbol{D}^{IJ} = \frac{1}{c^I|\Omega|}\int_\Omega \int \boldsymbol{\chi}^{\boldsymbol{I}}(\boldsymbol{x})\boldsymbol{\chi}^{\boldsymbol{J}}(\boldsymbol{x})\boldsymbol{\Phi}^0(\boldsymbol{x},\boldsymbol{x}')d\boldsymbol{x}'d\boldsymbol{x} \tag{13}$$

Where c^I is volume fraction of I-th cluster, while $\boldsymbol{\Phi}^0$ is Green's function. $\boldsymbol{\chi}^{\boldsymbol{I}}$ is characteristic function as Equation (5) shown.

Interaction tensor can be calculated by transform into Fourier coordinates as[71].

$$\phi^0_{ijkl} = \frac{1}{4\mu_0}\phi^1_{ijkl} - \frac{\lambda_0+\mu_0}{\mu_0(\lambda_0+2\mu_0)}\phi^2_{ijkl} \tag{14}$$

$$\phi^1_{ijkl} = \frac{\delta_{ik}\xi_j\xi_l + \delta_{il}\xi_j\xi_k + \delta_{jl}\xi_i\xi_k + \delta_{jk}\xi_i\xi_l}{|\boldsymbol{\xi}|^2}$$

$$\phi^2_{ijkl} = \frac{\xi_i\xi_j\xi_k\xi_l}{|\boldsymbol{\xi}|^4}$$

Where $\boldsymbol{\xi}$ is Fourier coordinates and λ_0 and μ_0 are lame parameter of reference material respectively. In Equation (14), Green's function is only determined by lame parameter of reference material and Fourier coordinates, so interaction tensor $\boldsymbol{D}^{IJ}$ can be calculated in advance to save calculation time.

2.2.3 Cluster-based Iterative Self-consistent Analysis

In order to achieve accurate results, two critical points must be discussed. Firstly, the choice of reference material stiffness $\boldsymbol{L}^{\boldsymbol{0}}$ and

secondly, the algorithmic details of the iterative solution for Equation (27).

It is noteworthy that the local strain ε(x) obtained from the continuous Lippmann-Schwinger equation, Equation (27), is independent of the reference stiffness $\boldsymbol{L^0}$. However, the convergence rate of the iterative solution scheme for the discrete Lippmann-Schwinger equation is impacted by the chosen $\boldsymbol{L^0}$. Nevertheless, despite the influence on convergence rate, the converged solution should be independent of $\boldsymbol{L^0}$ and identical regardless of its choice. $\boldsymbol{L^0}$ can be considered a preconditioner for the iterative scheme, as the physical problem is determined by the equilibrium condition and macroscopic constraints. Therefore, in theory, any reference stiffness $\boldsymbol{L^0}$ for the homogeneous linear elastic material can be selected.

In this chapter, algorithm with a constant $\boldsymbol{L^0}$ and updated $\boldsymbol{L^0}$ will be introduced respectively.

In this section, reference material $\boldsymbol{L^0}$ is considered as a constant matrix and will not be updated in iterations. The value of $\boldsymbol{L^0}$ is assumed as constitutive matrix of matrix material.

In many cases, such as plasticity and damage, the incremental stress in the I-th cluster ($\Delta\boldsymbol{\sigma}^I$) is a function of its incremental strain ($\Delta\boldsymbol{\varepsilon}^I$) as shown in Equation (15).

$$\Delta\boldsymbol{\varepsilon}^I + \sum_{J=1}^{k} \boldsymbol{D}^{IJ} : [\Delta\boldsymbol{\sigma}^J - \boldsymbol{C}^0 : \Delta\boldsymbol{\varepsilon}^J] - \Delta\boldsymbol{\varepsilon}^0 = \boldsymbol{0} \qquad (15)$$

This implies that the system of integral equations needs to be solved iteratively at every load increment. An implicit scheme is utilized for this purpose, considering both macro-strain and macro-stress constraints.

The unknown variables in the system are the incremental strain in each cluster ($\Delta\boldsymbol{\varepsilon}^I$) and the far-field strain ($\Delta\boldsymbol{\varepsilon}^0$), denoted by $\{\Delta\boldsymbol{\varepsilon}\} =$

$\{\Delta\boldsymbol{\varepsilon}^1, \ldots, \Delta\boldsymbol{\varepsilon}^k;\ \Delta\boldsymbol{\varepsilon}^0\}$. The problem is approached by defining the residual of the integral equation in the I-th cluster at iteration step n.

$$\boldsymbol{r}^I(\{\Delta\boldsymbol{\varepsilon}\}_n) = \Delta\boldsymbol{\varepsilon}_n^I + \sum_{I=1}^{k} \boldsymbol{D}^{IJ} : [\Delta\boldsymbol{\sigma}_n^J - \boldsymbol{L}^0 : \Delta\boldsymbol{\varepsilon}_n^J] - \Delta\boldsymbol{\varepsilon}_n^0 \tag{16}$$

Where I=1, 2, …, k. And the residual of micro-stress and micro-strain are.

$$\boldsymbol{r}^{k+1}(\{\Delta\boldsymbol{\sigma}\}_n) = \sum_{I=1}^{k} c^I\, \Delta\boldsymbol{\sigma}_n^I - \Delta\bar{\boldsymbol{\sigma}} \tag{17}$$

$$\boldsymbol{r}^{k+1}(\{\Delta\boldsymbol{\varepsilon}\}_n) = \sum_{I=1}^{k} c^I\, \Delta\boldsymbol{\varepsilon}_n^I - \Delta\bar{\boldsymbol{\varepsilon}}$$

The residual matrix is $\{\boldsymbol{r}\} = \{\boldsymbol{r}^1, \ldots, \boldsymbol{r}^k,\ \boldsymbol{r}^{k+1}\}$ and

$$\{\boldsymbol{r}\} + \{\boldsymbol{M}\}\{\delta\boldsymbol{\varepsilon}\} = \boldsymbol{0} \tag{18}$$

Where $\boldsymbol{M}$ is Jacobian matrix which can be calculated by

$$\boldsymbol{M}^{IJ} = \boldsymbol{\delta}_{IJ}\boldsymbol{I} + \boldsymbol{D}^{IJ} : \left(\boldsymbol{L}_{alg}^J - \boldsymbol{L}^0\right) \tag{19}$$

Where $\boldsymbol{\delta}_{IJ}$ is the Kronecker delta in terms of indices I and J. Additionally, the $\boldsymbol{L}_{alg}^J$ is the tangent modulus serves as a necessary output of the local constitutive law for the current strain increment within the designated J-th cluster as.

$$\boldsymbol{L}_{alg}^J = \frac{\partial\Delta\boldsymbol{\sigma}^J}{\partial\Delta\boldsymbol{\varepsilon}^J} \tag{20}$$

The other component of Jacobian matrix $\boldsymbol{M}$ under macro-strain is

$$\boldsymbol{M}^{(k+1)I} = c^I\boldsymbol{I} \tag{21}$$
$$\boldsymbol{M}^{(k+1)(k+1)} = \boldsymbol{0}$$

While Jacobian matrix under macro-stress is

$$\boldsymbol{M}^{(k+1)I} = c^I\boldsymbol{L}_{alg}^I \tag{22}$$
$$\boldsymbol{M}^{(k+1)(k+1)} = \boldsymbol{0}$$

Based on the latest incremental strain data, the constitutive relationship within each cluster can be utilized to calculate the updated incremental stress $\{\Delta\boldsymbol{\sigma}\} = \{\Delta\boldsymbol{\sigma}^1, \ldots, \Delta\boldsymbol{\sigma}^k;\ \Delta\boldsymbol{\sigma}^0\}$. The implicit scheme algorithm, stresses that the constant $\boldsymbol{L}^0 = \boldsymbol{L}^{input}$ is chosen as an input parameter. It is recommended that the effective stiffness of the RVE determined in the offline stage, $\boldsymbol{L}^{input} = \boldsymbol{L}^{macro}$, be considered as the reference value. However, other reference stiffnesses, such as the

stiffness of the matrix phase, $\boldsymbol{L}^{input} = \boldsymbol{L}^{matrix}$, can also be considered. Maintaining a formal tone, these alterations will significantly enhance the professionalism of the essay.

Instead of the constant reference material $\boldsymbol{L^0}$, the $\boldsymbol{L^0}$ considered as variable which is updated in each iteration is adopted.

In order to maintain the simplicity and convenience of utilizing the same form of Green's functions during plasticity, the tangent modulus $\boldsymbol{L}^{macro}$is often considered to be isotropic, even in cases where plastic flow may lead to anisotropic behavior, particularly when subjected to large deformations. However, it is important to note that this assumption is not universally valid.

When approaching each macroscopic load increment, the self-consistent scheme must determine two Lame parameters, namely λ_n^0 and μ_n^0, which are independent of one another and are used to define $\boldsymbol{L}_n^0$ at n-th increment. By assuming isotropy in the reference tangent modulus at each incremental load stage, the scheme is then able to determine the appropriate values for these parameters.

$$\boldsymbol{L}_n^0 = f(\lambda_n^0, \mu_n^0) \tag{23}$$

The self-consistent analysis is to find minimization as

$$\{\lambda_n^0, \mu_n^0\} = argmin\|\Delta\sigma_n^{macro} - f(\lambda', \mu'):\Delta\varepsilon_n^{macro}\|^2 \tag{24}$$

Here, Newton Raphson's iteration can be adopted to get the non-linear iterations as.

$$g(\lambda_n^0, \mu_n^0) = \|\Delta\sigma_n^{macro} - f(\lambda_n^0, \mu_n^0):\Delta\varepsilon_n^{macro}\|^2 \tag{25}$$

With calculating partial derivatives

$$\frac{\partial g}{\partial\lambda_n^0}\Big|_{\lambda_{opt}^0,\mu_{opt}^0} = 0, \frac{\partial g}{\partial\mu_n^0}\Big|_{\lambda_{opt}^0,\mu_{opt}^0} = 0 \tag{26}$$

The system presents an exclusive solution, except when subjected to a pure shear loading condition, whereby the value of λ_{opt}^0 becomes underdetermined. Consequently, λ_n^0 remains unaltered. Furthermore, the values of $g(\lambda_n^0, \mu_n^0)$ become negligible when the

effective macroscopic homogeneous material is isotropic linear elastic in nature.

This particular homogenization scheme is referred to as a self-consistent scheme, which means that it is iterative in nature. This is due to the fact that the macroscopic incremental stress ($\Delta\sigma_n^{macro}$ and strain ($\Delta\varepsilon_n^{macro}$) present at the beginning of each increment are calculated based on previous values of λ_n^0 and μ_n^0. It is important to note that when implementing the algorithm using a constant $\boldsymbol{L^0}$, the tangent modulus is not updated. Therefore, the interaction tensors $\boldsymbol{D^{IJ}}$ also do not need to be updated. Conversely, with the self-consistent algorithm, the interaction tensors are contingent upon updated reference Lame parameters as Equation (7), which requires the updating of said parameters Equation (14).

2.3. Mori-Tanaka Homogenization

The Mori-Tanaka (MT) method, proposed in 1981, has become a widely used and classical approach for predicting the effective stiffness of composite materials. Over the years, extensive research has been conducted to extend and apply the MT method in various contexts [72-74]. Researchers have explored its application in thermo-elasto-plastic constitutive laws with an incremental formulation [75-80], considered interface debonding models [81, 82], and investigated the homogenization of elastic-viscoplastic heterogeneous materials [56]. Furthermore, the MT method has been combined with self-consistent approaches [83] and utilized for predicting effective thermal conductivity [84, 85].

The MT model has found application in diverse areas, such as CNT nanocomposites [86-88], functionally graded materials [89-91], and porous materials [90]. The Eshelby tensor within the MT method has been employed in these studies to describe reinforcing inclusions with interphase weaknesses, as weakened interfaces are commonly observed [92]. Many researchers have adopted the linear spring model for interface damage between CNT and polymer matrices [93-95]. Recently, Ryu et al. identified

and rectified mathematical and typographical errors in the interfacial damage tensor denoted by Q in previous studies [96].

Additionally, investigations on stochastic effects have been conducted to understand the influence of CNT inclusion waviness and its distribution on effective stiffness [97]. Shao et al. focused on the waviness of CNTs and interface debonding behavior, two key factors influencing reinforcing efficiency[14].

These studies collectively highlight the wide range of applications and advancements in utilizing the MT method, along with its extension to encompass various phenomena and material systems. By leveraging the MT method and considering factors such as interfacial damage and waviness, researchers have made significant progress in understanding and predicting the mechanical behavior of composite materials, particularly CNT nanocomposites.

Mori-Tanaka homogenization is a widely used technique for predicting the effective or average mechanical properties of heterogeneous materials. This method was developed by T. Mori and K. Tanaka in the year 1973[72]. The homogenization approach approximates the behavior of complex composites by using simplified assumptions and models with reduced complexity. The main advantage of Mori-Tanaka homogenization is that it can predict the mechanical behavior of a composite material from the properties of its constituent materials. This allows for the design of materials with specific mechanical properties, such as high strength, stiffness, and fracture toughness. To achieve this, the Mori-Tanaka method uses the concept of representative volume elements (RVEs) to represent the composite material and simplify the complex interactions between its constituents.

Similar with homogenization model described in Chapter 3, the equilibrium can be expressed as

$$\Delta\boldsymbol{\varepsilon}^{I} + \sum_{J=1}^{k} \boldsymbol{D}^{IJ} : [\Delta\boldsymbol{\sigma}^{J} - \boldsymbol{C}^{0} : \Delta\boldsymbol{\varepsilon}^{J}] - \Delta\boldsymbol{\varepsilon}^{0} = \mathbf{0} \qquad (27)$$

The strain concentration tensor is defined as

$$\boldsymbol{a}^I = [\boldsymbol{I} + \boldsymbol{D}^{II} : \Delta \boldsymbol{L}^I]^{-1} \left(\boldsymbol{I} - \sum_{\substack{J=1 \\ J \neq I}}^{N} \boldsymbol{D}^{IJ} : \Delta \boldsymbol{L}^J : \boldsymbol{a}^J \right) \tag{28}$$

Unlike the cluster-based Lippmann Schwinger Equation, the I, J=1…N indicates N phases of composites. It is important to note that the phase refers to the constituent materials of composites, whereas clusters is related to the microstructure of composites. Typically, composites materials are composed of several materials, thus they consist of multiple phases. On the other hand, the clusters are determined by grouping similar elements of elastic response under boundary condition. The SMC are regarded as one-site composites, which assume the interaction tensor $\boldsymbol{D}^{IJ}$ to be 0. The global strain concentration tensor is[98].

$$\boldsymbol{A}^I = \boldsymbol{a}^I : (\overline{\boldsymbol{a}}^I)^{-1} = \boldsymbol{a}^I : \boldsymbol{A}^0 \tag{29}$$

Where $\overline{\boldsymbol{a}}^I$ is the volume averaging of local strain concentration tensor $\boldsymbol{a}^I$. Equation (29) establishes a crucial link between macro- and micro-scale modeling of strain concentration in composite materials, serving as a bridge between the two domains.

$$\varepsilon_{ij}(x) = A_{ijkl}(x) : E_{kl} \tag{30}$$

Specifically, this equation represents the relationship between global and local strain concentration tensors, providing a means of connecting the macroscopic behavior of a composite material with its underlying microstructure.

As a results, the homogenized composites RVE is calculated by volume averaging of elastic constitutive matrix.

$$L_{ijkl}^{eff} = \frac{1}{V} \int_V l_{ijmn}(x) A_{mnkl}(x) dV \tag{31}$$

Combining Equation (28), (29) and (31), the constitutive matrix for composites of Mori-Tanaka model is calculated as.

$$\boldsymbol{L}_{MT}^{eff} = c^0 \boldsymbol{L}^0 + \sum_{I=1}^{N} c^I \boldsymbol{L}^I \boldsymbol{A}^I \tag{32}$$

2.4. Improved Mori-Tanaka Homogenization

2.4.1 Mori-Tanaka Homogenization with Interface Damage

In this section, damage analysis of the composite material is adopted. The composite is composed of two phases, the matrix (0^{th} phase) and the CNT (1^{st} phase). The CNT fibers are assumed to be long circular cylindrical inclusions in a homogenized matrix material (D), treated as a sub-domain (Ω). The original Mori-Tanaka (MT) effective stiffness model assumes that the inclusions are unidirectionally aligned. When a uniform far-field applied strain ($(\boldsymbol{\varepsilon}_a)$) is applied to the homogeneous matrix, it exhibits a homogeneous strain field. However, the addition of inclusions results in perturbed inclusion strains, causing the average matrix strain $\langle \boldsymbol{\varepsilon}_0 \rangle$ to differ from the average inclusion strain $\langle \boldsymbol{\varepsilon}_1 \rangle$ by the perturbed inclusion strain, $\boldsymbol{\varepsilon}_1^{pt}$, as follows.

$$\langle \boldsymbol{\varepsilon}_1 \rangle = \langle \boldsymbol{\varepsilon}_0 \rangle + \boldsymbol{\varepsilon}_1^{pt} = \langle \boldsymbol{\varepsilon}_0 \rangle + \boldsymbol{S}\boldsymbol{\varepsilon}_1^{*} \tag{33}$$

Where $\langle \cdot \rangle$ indicates values from volume averaging over the entire composite domain (D); $\boldsymbol{\varepsilon}_1^{*}$ is the fictitious eigenstrain of inclusion in Ω; and $\boldsymbol{S}$ is the uniform 4th order Eshelby inclusion tensor. The equivalent inclusion method can simulate inclusion stress $(\langle \boldsymbol{\varepsilon}_1 \rangle)$ by elastic stiffness $(\boldsymbol{L}_0)$ of the matrix and fictitious eigenstrain $\boldsymbol{\varepsilon}_1^{*}$ in Ω as follows. The relation between both coordinate system with rotational angle was shown in Figure 2. z' axis of material coordinate system aligns in x-y plane of a global coordinate system.

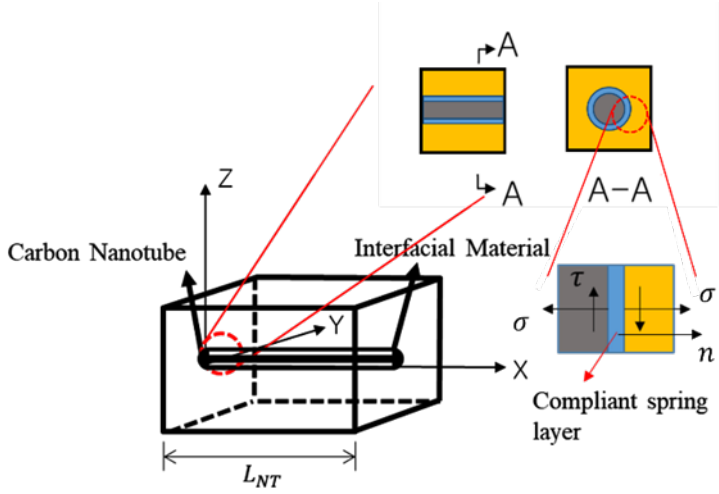

(a)

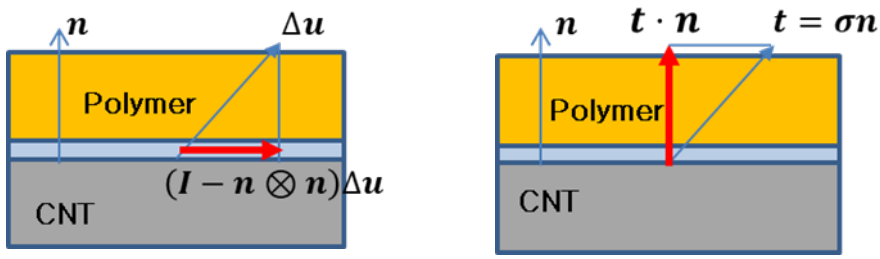

(b) (c)

Figure 2. (a) spring layer modeling of interphase (b) tangential component of discontinuous displacement (c) normal component of the traction

$$\boldsymbol{\varepsilon}_1^* = -\boldsymbol{L}_0^{-1}(\boldsymbol{L}_1 - \boldsymbol{L}_0)\langle\boldsymbol{\varepsilon}_1\rangle \tag{34}$$

Substituting Equation (28) into Equation (27), derive the relationship between $\langle\boldsymbol{\varepsilon}_1\rangle$ and $\langle\boldsymbol{\varepsilon}_0\rangle$ with the dilute strain concentration tensor $\boldsymbol{A}_1$ as follows.

$$\langle\boldsymbol{\varepsilon}_1\rangle = \boldsymbol{A}_1\langle\boldsymbol{\varepsilon}_0\rangle = [\boldsymbol{I} + \boldsymbol{S}\boldsymbol{L}_0^{-1}(\boldsymbol{L}_1 - \boldsymbol{L}_0)]^{-1}\langle\boldsymbol{\varepsilon}_0\rangle \tag{35}$$

where $\boldsymbol{I}$ is the fourth order identity tensor. Equation (35) relates the average strain in the inclusion $\langle\boldsymbol{\varepsilon}_1\rangle$ to the average strain in the matrix $\langle\boldsymbol{\varepsilon}_0\rangle$ by the dilute strain concentration tensor. Accounting for the inclusion interaction, the applied strain for each inclusion is the average strain in the matrix $\langle\boldsymbol{\varepsilon}_0\rangle$ instead of the far field applied

strain($\boldsymbol{\varepsilon_0}$). This implies that the average inclusion strain is defined as follows.

$$\langle \boldsymbol{\varepsilon}_1 \rangle = \boldsymbol{A}_1 \boldsymbol{\varepsilon}_a \tag{36}$$

By the equal stress assumption $c_0\langle \boldsymbol{\varepsilon_0} \rangle + c_1 \langle \boldsymbol{\varepsilon_1} \rangle = \boldsymbol{\varepsilon_a}$, the average strain in the matrix is related to the applied strain as follows.

$$\langle \boldsymbol{\varepsilon}_0 \rangle = \boldsymbol{A}_0 \boldsymbol{\varepsilon}_a = [c_0 \boldsymbol{I} + c_1 \boldsymbol{A}_1]^{-1} \boldsymbol{\varepsilon}_a \tag{37}$$

Where c_0 and c_1 are the volume fractions of matrix and CNT, respectively. Then the effective elastic stiffness matrix of the MT model can be derived from the equal strain relationship $\langle \boldsymbol{\sigma}_0 \rangle = c_0 \langle \boldsymbol{\sigma}_0 \rangle + c_1 \langle \boldsymbol{\sigma}_1 \rangle = \boldsymbol{L} \boldsymbol{\varepsilon}_a$ by substituting Hooke's law.

$$\boldsymbol{L} = [c_0 \boldsymbol{L}_0 + c_1 \boldsymbol{L}_1 \boldsymbol{A}_1][c_0 \boldsymbol{I} + c_1 \boldsymbol{A}_1]^{-1} \tag{38}$$

Where $\boldsymbol{A}_1 = \left[\boldsymbol{I} + \boldsymbol{S}\boldsymbol{L}_0^{-1}(\boldsymbol{L}_1 - \boldsymbol{L}_0)\right]^{-1}$.

On the other hand, the Eshelby tensor for a long circular cylindrical fiber (i.e. CNT) is given as follows[99].

$$\begin{aligned} S_{1111} &= S_{1122} = S_{1133} = 0 \\ S_{2222} &= S_{3333} = \frac{5 - 4v_0}{8(1 - v_0)} \\ S_{2211} &= S_{3311} = \frac{v_0}{2(1 - v_0)} \\ S_{2233} &= S_{3322} = \frac{4v_0 - 1}{8(1 - v_0)} \\ S_{1212} &= S_{1313} = \frac{1}{4} \\ S_{2323} &= \frac{v_0}{8(1 - v_0)} \end{aligned} \tag{39}$$

Where v_0 is the Poisson ratio of the matrix. When calculating S_{ijkl}, Eshelby neglected the situation of interfacial debonding which means the perfect bonding between inclusions and matrix was assumed.

To consider imperfect interfacial bonding, a compliant spring layer with zero thickness is assumed to simulate continuous traction and discontinuous displacement along the interface as shown in

Figure 2. MT modeling approach for weakened interfacial damage in a reference [91] was referred in this thesis.

The compliance tensor for the single-layered interface is given as follows[91].

$$\eta = \alpha\delta_{ij}[e_i \otimes e_j] + (\beta - \alpha)n_i n_j[e_i \otimes e_j] \quad (40)$$

Where δ_{ij} is the Kronecker delta; η is the compliance tensor of the interface; and n_i is the outward normal vector to the interfacial surface between matrix and inclusion. α and β indicate compliance in the tangential and normal directions of the interface, respectively as defined in Equation (40).

$$(\boldsymbol{I} - \boldsymbol{n} \otimes \boldsymbol{n})\Delta\boldsymbol{u} = \alpha(\boldsymbol{I} - \boldsymbol{n} \otimes \boldsymbol{n})\boldsymbol{\sigma n} \quad (41)$$
$$\Delta\boldsymbol{u} \cdot \boldsymbol{n} = \beta\boldsymbol{\sigma n} \cdot \boldsymbol{n}$$

Where $(\boldsymbol{I} - \boldsymbol{n} \otimes \boldsymbol{n})$ is the projection tensor projected onto the interfacial surface; Δu is the displacement vector on the interface; $\boldsymbol{\sigma n}(= \boldsymbol{t})$ is the traction vector by Cauchy stress formula; and $\boldsymbol{I}$ is the identity tensor. When $\eta_{ij} = 0$, there is no debonding between inclusion and matrix. When $\eta_{ij} \to \infty$ (i.e. zero stiffness), perfect debonding is applied.

In the case of imperfect interface, the inclusion strain field becomes non-uniform. By virtue of the Green's function in an infinite domain, the inclusion strain field with the weakened interface is obtained through modification of the original Eshelby solution[91, 100].

$$\varepsilon_{ij}(\boldsymbol{x}) = S_{ijkl}\varepsilon^*_{kl} - L_{klmn}\int_{\partial\Omega}\eta_{kp}\sigma_{pk}(\boldsymbol{\xi})G_{ijmn}(\boldsymbol{\xi} - \boldsymbol{n})n_q n_l dS(\boldsymbol{\xi}) \quad (42)$$

Where $\partial\Omega$ is the surface of the inclusion domain and G_{ijmn} is the function of the Green's function[91]. Certainly when $\eta_{kp} = 0$, the inclusion strain field becomes the original Eshelby equation, and the inclusion strain is no longer uniform. Qu obtained the modified Eshelby tensor $\bar{S}^I_{ijkl}$ for the inclusion with the slightly weakened interface as follows[91].

$$\overline{\boldsymbol{S}}^I = \boldsymbol{S} + (\boldsymbol{I} - \boldsymbol{S}) : \boldsymbol{H} : \boldsymbol{L}_0(\boldsymbol{I} - \boldsymbol{S}) \quad (43)$$

Where $\boldsymbol{L_0}$ is the effective stiffness of matrix material. $\boldsymbol{H}$ can be calculated in terms of the interfacial compliances as follows[91].

$$H_{ijkl} = \alpha P_{ijkl} + (\beta - \alpha) Q_{ijkl} \tag{44}$$

Where P_{ijkl} and Q_{ijkl} are tensors that depend on the shape of inclusions. Original inclusion by Eshelby was an ellipsoidal shape of which domain is expressed by $\left(\frac{x_1}{a_1}\right)^2 + \left(\frac{x_2}{a_2}\right)^2 + \left(\frac{x_3}{a_3}\right)^2 \leq 1$, where a_1, a_2 and a_3 are principal semi-axes of ellipsoid. Ellipsoids can be specified to spherical and cylindrical inclusion shapes. In this case, inclusion is CNT fiber considered as a cylinder ($a_1 = a_2 = a$ and $a_3 \to \infty$) of which $\boldsymbol{P}$ and $\boldsymbol{Q}$ tensors are determined as follows[91], and here a is the radius of CNT inclusion. Having $a_3 \to \infty$ is the reason that the aspect ratio cannot be specified in the MT model, which will be explained later.

$$P_{1111} = P_{2222} = 4P_{2323} = 4P_{1313} = 2P_{1212} = \frac{3\pi}{8a} \tag{45}$$

$$Q_{1111} = Q_{2222} = 3Q_{1122} = 3Q_{2211} = 3Q_{1212} = \frac{9\pi}{32a}$$

$$Others = 0$$

Then the effective stiffness can be calculated for CNT reinforced nanocomposites with interfacial damage as follows[91].

$$\bar{\boldsymbol{L}}^{\boldsymbol{I}} = (c_0\boldsymbol{L}_0 + c_1\boldsymbol{L}_1\boldsymbol{A}_1^I)(c_0\boldsymbol{I} + c_1\boldsymbol{A}_1^I + c_1\boldsymbol{H}\boldsymbol{L}_1\boldsymbol{A}_1^I)^{-1} \tag{46}$$

For the perfect bonding, α and β are zero and the tensor H becomes zero. Therefore, Equation (17) will become the original MT model.

2.4.2 Mori-Tanaka Homogenization with random wavy fiber

After completing the strain concentration tensor $\boldsymbol{A}^I$ with interfacial damage, next is to derive the wavy CNT fiber,

An alternative form for the MT model can also be obtained as follows[72, 101].

$$\boldsymbol{L} = \boldsymbol{L}_0(\boldsymbol{I} + c_1[(\boldsymbol{L}_1 - \boldsymbol{L}_0)^{-1}\boldsymbol{L}_0 + c_0\bar{\boldsymbol{S}}]^{-1}) \tag{47}$$

Where $\bar{\boldsymbol{S}}$ is the Eshelby tensor that represents perfect interface bonding. Substituting the Eshelby tensor of Equation (15) into the alternative form of the MT Model in Equation (32), the effective elastic stiffness of composites with interface damage is obtained as follows.

$$\bar{\boldsymbol{L}}^{I} = \boldsymbol{L}_0(\boldsymbol{I} + c_1[(\boldsymbol{L}_1 - \boldsymbol{L}_0)^{-1}\boldsymbol{L}_0 + c_0\bar{\boldsymbol{S}}^{I}]^{-1}) \tag{48}$$

Where $\bar{\boldsymbol{S}}^{I}$ is the Eshelby tensor containing interface damage in Equation (42). This effective stiffness $\bar{\boldsymbol{L}}^{I}$ was verified to provide the same elastic stiffness matrix as one from Equation (48) for a set of specific damage variables (i.e. α and β). Following the analytical approach by Hsiao and Daniel [102] and Yanase et al, [103] in order to calculate the effective elastic stiffness of wavy CNT composites with interface weakened, wavy CNT is modeled in a sinusoidal shape as depicted in Figure 3.

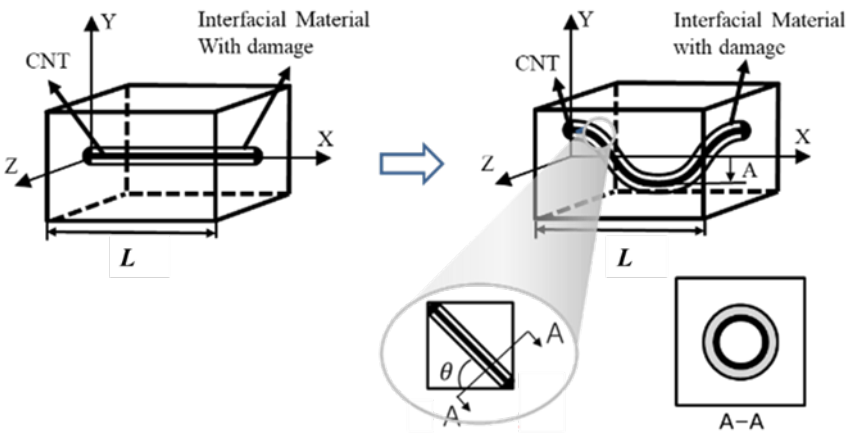

Figure 3. Modeling of wavy fiber with interface damage

The sinusoidal waviness of CNT is defined in terms of the length L and amplitude A as follows.

$$v = A\sin\left(\frac{2\pi x}{L}\right) \tag{49}$$

$$a = \frac{2\pi A}{L} = 2\pi w$$

Where w is waviness. A rotational transformation of $\bar{\boldsymbol{L}}^{I}$ and averaged along the sinusoidal CNT fiber are obtained and the effective stiffness $\bar{\boldsymbol{L}}^{IW}$ of composites with interface weakened and wavy unidirectional CNT.

$$\bar{L}^{IW}_{\alpha\beta\gamma\delta} = \frac{1}{l}\int_0^l R_{i\alpha}R_{\beta j}R_{\gamma k}R_{\delta l}\bar{L}^{I}_{ijkl}dx \tag{50}$$

Where $[R_{ij}] = \begin{bmatrix} cos\,\theta & -sin\,\theta & 0 \\ sin\,\theta & cos\,\theta & 0 \\ 0 & 0 & 1 \end{bmatrix}$

Where θ is the tangential angle along the sinusoidal CNT as depicted in Figure 3. To conduct the averaging and rotational transforming in Equation (50) along a single inclusion fiber, relating the angle θ to the waviness parameters A and L as follows.

$$tan\,\theta = a\,cos\frac{2\pi x}{L} \tag{51}$$

$$m = cos\,\theta = \left[1 + \left(a\,cos\frac{2\pi x}{L}\right)^2\right]^{-1/2}$$

$$n = sin\,\theta = a\,cos\frac{2\pi x}{L}\left[1 + \left(a\,cos\frac{2\pi x}{L}\right)^2\right]^{-1/2}$$

The integration in Equation (50) can be explicitly expressed as

$$\frac{1}{L}\int_0^L m^4 dx = \frac{2+a^2}{2(1+a^2)^{3/2}} = I_1 \tag{52}$$

$$\frac{1}{L}\int_0^L m^2 n^2 dx = \frac{a^2}{2(1+a^2)^{1/2}} = I_2$$

$$\frac{1}{L}\int_0^L m^2 dx = \frac{1}{(1+a^2)^{1/2}} = I_1 + I_2$$

$$\frac{1}{L}\int_0^L n^2 dx = 1 - \frac{1}{(1+a^2)^{3/2}} = 1 - I_1 - I_2$$

$$\frac{1}{L}\int_0^L m^3 n dx = \frac{1}{L}\int_0^L m n^3 dx = \frac{1}{L}\int_0^L mn dx = 0$$

Components of the transformed stiffness matrix in Equation (45) are expressed explicitly as follows.

$$\bar{L}^{IW}_{1111} = I_1(\bar{L}^{I}_{1111} - \bar{L}^{I}_{2222}) + 2I_2(\bar{L}^{I}_{1122} - \bar{L}^{I}_{2222} + 2\bar{L}^{I}_{1212}) + \bar{L}^{I}_{2222} \tag{53}$$

$$\bar{L}^{IW}_{1111} = I_1(\bar{L}^{I}_{1111} - \bar{L}^{I}_{2222}) + 2I_2(\bar{L}^{I}_{1122} - \bar{L}^{I}_{2222} + 2\bar{L}^{I}_{1212}) + \bar{L}^{I}_{2222}$$

$$\bar{L}^{IW}_{1122} = I_2(\bar{L}^{I}_{1111} - 2\bar{L}^{I}_{1122} + \bar{L}^{I}_{2222} - 4\bar{L}^{I}_{1212}) + \bar{L}^{I}_{1122}$$

$$\bar{L}^{IW}_{1133} = I_1(\bar{L}^{I}_{1122} - \bar{L}^{I}_{2233}) + I_2(\bar{L}^{I}_{1122} - \bar{L}^{I}_{2233}) + \bar{L}^{I}_{2233}$$

$$\bar{L}^{IW}_{2211} = I_1(\bar{L}^{I}_{1111} - 2\bar{L}^{I}_{1122} + \bar{L}^{I}_{2222} - 4\bar{L}^{I}_{1212}) + \bar{L}^{I}_{1122}$$

$$\bar{L}^{IW}_{2222} = I_1(\bar{L}^{I}_{2222} - \bar{L}^{I}_{1111}) + I_2(2\bar{L}^{I}_{1122} - 4\bar{L}^{I}_{1212} - 2\bar{L}^{I}_{1111}) + \bar{L}^{I}_{1111}$$

$$\bar{L}^{IW}_{2233} = I_1(\bar{L}^{I}_{2233} - \bar{L}^{I}_{1122}) + I_2(\bar{L}^{I}_{2233} - \bar{L}^{I}_{1122}) + \bar{L}^{I}_{1122}$$

$$\bar{L}^{IW}_{3311} = (I_1 + I_2)(\bar{L}^{I}_{1122} - \bar{L}^{I}_{2233}) + \bar{L}^{I}_{2233}$$

$$\bar{L}^{IW}_{3322} = (I_1 + I_2)(\bar{L}^{I}_{2233} - \bar{L}^{I}_{1122}) + \bar{L}^{I}_{1122}$$

$$\bar{L}^{IW}_{3333} = \bar{L}^{I}_{3333}$$

$$\bar{L}^{IW}_{1212} = I_2(\bar{L}^{I}_{1111} - 2\bar{L}^{I}_{1122} + \bar{L}^{I}_{2222} - 4\bar{L}^{I}_{1212}) + \bar{L}^{I}_{1212}$$

$$\bar{L}^{IW}_{2323} = (I_1 + I_2)(\bar{L}^{I}_{2323} - \bar{L}^{I}_{1212}) + \bar{L}^{I}_{1212}$$

$$\bar{L}^{IW}_{1313} = (I_1 + I_2)(\bar{L}^{I}_{1212} - \bar{L}^{I}_{2323}) + \bar{L}^{I}_{2323}$$

Substituting $\bar{\boldsymbol{L}}^{IW}$ of Equation (53) into $\bar{\boldsymbol{L}}^{I}$ of Equation (49), we can obtain the MT model for wavy CNT nanocomposites with interface damage as follows.

$$\bar{\boldsymbol{L}}^{IW} = \boldsymbol{L}_0(\boldsymbol{I} + c_1[(\boldsymbol{L}_1 - \boldsymbol{L}_0)^{-1} + c_0\bar{\boldsymbol{S}}^{IW}]^{-1}) \tag{54}$$

Then the Eshelby tensor $\bar{\boldsymbol{S}}^{I}$ changes to $\bar{\boldsymbol{S}}^{IW}$accordingly. The Eshelby tensor $\bar{\boldsymbol{S}}^{IW}$ is for CNT inclusions with both interfacial damage and waviness. Then, back-calculate the Eshelby tensor $\bar{S}^{IW}$ for wavy CNT with interface damage as follows.

$$\bar{\boldsymbol{S}}^{IW} = \lim_{c_1\to\infty} \frac{1}{1-c_1}\left[c_1\left(\boldsymbol{L}_0{}^{-1}\bar{\boldsymbol{L}}^{IW} - \boldsymbol{I}\right)^{-1} - (\boldsymbol{L}_1 - \boldsymbol{L}_0)^{-1}\boldsymbol{L}_0\right] \tag{55}$$

Applying the modified Eshelby tensor in Equation (55), we can also obtain the effective elastic stiffness as follows.

$$\bar{\boldsymbol{L}}^{IW} = (c_0\boldsymbol{L}_0 + c_1\boldsymbol{L}_1\boldsymbol{A}_1^{IW})(c_0\boldsymbol{I} + c_1\boldsymbol{A}_1^{IW})^{-1} \tag{56}$$
$$\boldsymbol{A}_I^{IW} = [\boldsymbol{I} + \bar{\boldsymbol{S}}^{IW}\boldsymbol{L}_0^{-1}(\boldsymbol{L}_1 - \boldsymbol{L}_0)]^{-1}$$

An alternative form for the effective stiffness of wavy CNT nanocomposites with interface weakened is also introduced as follows.

$$\bar{\boldsymbol{L}}^{IW} = (c_0\boldsymbol{L}_0 + c_1\boldsymbol{L}_1\boldsymbol{A}_1^{W})(c_0\boldsymbol{I} + c_1\boldsymbol{A}_1^{W} + c_1\boldsymbol{H}\boldsymbol{L}_1\boldsymbol{A}_1^{W})^{-1} \tag{57}$$
$$\boldsymbol{A}_1^{W} = [\boldsymbol{I} + \bar{\boldsymbol{S}}^{W}\boldsymbol{L}_0^{-1}(\boldsymbol{L}_1 - \boldsymbol{L}_0)]^{-1}$$

Where $\bar{\boldsymbol{S}}^{W} = \lim_{c_1\to\infty} \frac{1}{1-c_1}[c_1(\boldsymbol{L}_0^{-1}\bar{\boldsymbol{L}}^{W} - \boldsymbol{I})^{-1} - (\boldsymbol{L}_1 - \boldsymbol{L}_0)^{-1}\boldsymbol{L}_0]$

According to the tests, effective stiffness matrices of Equation (56) and (57) are identical. These MT models are for unidirectional aligned CNT nanocomposites as shown in Figure 4(a). However, in

most cases, actual CNT fibers are randomly oriented as in Figure 4(b).

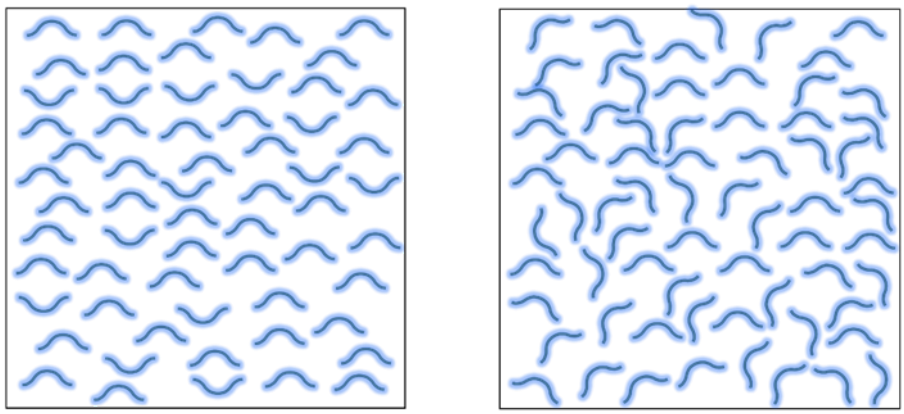

(a) (b)

Figure 4. (a) unidirectional aligned wavy CNT distribution (b) randomly oriented wavy CNT distribution

2.4.3 Mori-Tanaka Homogenization with plasticity and ductile damage

In Section 2.4.3, it is presented an improved method to simulate the behavior of carbon nanotube (CNT) nanocomposites in the elastic range. However, it is also important to consider the situation where plasticity occurs. When plasticity occurs, the strain-stress curve becomes nonlinear, and the plastic effective properties become related to the hardening function, plastic strain, and ductile damage. Therefore, the elasto-plastic properties of composites have always been of great interest to researchers. Elasto-plasticity is not only important for simulating material properties after composite damage, but it is also more realistic in research experiments and production processes. In their work, Azoti et al. [104] provided an elasto-plastic constitutive model with an incremental micromechanics scheme. To further improve the understanding of the plasticity of CNT nanocomposites, additional research have been conducted in modeling the plastic behavior of these composites with interface and ductile damage in the matrix phase since damage is an inevitable element in simulations.

In Section 2.4.1, it is presented a nonlinear composites model in the plastic range using the Mori-Tanaka method with interfacial and ductile damage introduced through the use of the Lemaitre-Chaboche damage modeling method. As the effective properties difference between the matrix and inclusion is usually significant, it is assumed that the inclusion is always elastic during the simulation, while the matrix becomes plastic with increasing strain. Additionally, propose a multiscale transformation is proposed to achieve macro stress and strain increments. By developing these models, simulation of the behavior of CNT nanocomposites in the plastic range is more accurate, which will provide valuable insights into the material properties and behavior of these composites.

For CNT nanocomposites, it is considered two phases, CNT inclusion and polymer matrix and boundary condition and kinematic loadings are in macro scope.

Global strain concentration tensor $\boldsymbol{A}$ is defined by Equation (58) and links local strain with macroscopic strain $\boldsymbol{E}$

$$\boldsymbol{e}(\boldsymbol{r}) = \boldsymbol{A}(r) : \boldsymbol{E} \tag{58}$$

Dederichs and Zeller [68] provided the kinematic integral equation as

$$\boldsymbol{\varepsilon}(\boldsymbol{r}) = \boldsymbol{E}^{R}(\boldsymbol{r}) - \int_{V} \Gamma(\boldsymbol{r} - \boldsymbol{r}') : \delta\boldsymbol{c}(\boldsymbol{r}')dVE \tag{59}$$

where $\boldsymbol{\varepsilon}(\boldsymbol{r})$ is the local strain, $\Gamma(\boldsymbol{r} - \boldsymbol{r}')$ is the modified Green tensor and $\boldsymbol{E}^{R}$ is the strain field in the reference infinite medium. Also $\boldsymbol{c}(\boldsymbol{r}')$ indicates the local effective stiffness, and the integration is over the Representative Volume Element (RVE) with volume V.

Then, can get

$$\boldsymbol{\varepsilon}^{I}(\boldsymbol{r}) = \boldsymbol{a}^{I}(\boldsymbol{r}) : \boldsymbol{E}^{R} \tag{60}$$

where $\boldsymbol{a}^{I}(\boldsymbol{r})$ is the local strain concentration tensor which relates the local stress with strain field in the reference medium. Based on the theory proposed by Vieville[98], the global strain concentration tensor is

$$\boldsymbol{A}^{I}(\boldsymbol{r}) = \boldsymbol{a}^{I}(\boldsymbol{r}) : (\bar{\boldsymbol{a}}^{I})^{-1} \tag{61}$$

where $\bar{\boldsymbol{a}}^I$ is the volume mean local concentration tensor which in two-phase composites with interfacial damage can be expressed as

$$\bar{\boldsymbol{a}}^I = c_0\boldsymbol{a}^0 + c_1\boldsymbol{a}^1 + c_1\boldsymbol{H}^1\boldsymbol{L}_1\boldsymbol{a}^1 \qquad (62)$$
$$\boldsymbol{A}^0 = (\bar{\boldsymbol{a}}^I)^{-1}$$

where $\boldsymbol{H}^1$ is the interfacial damage tensor which mentioned in Section 2.4.1, And c_0 and c_1 are the volume fraction of inclusion and matrix, respectively.

In the case of one site simulation, local strain concentration $\boldsymbol{a}^I$ is given as

$$\boldsymbol{a}^I = [\boldsymbol{I} + \boldsymbol{S}:(\boldsymbol{L_0})^{-1}:(\boldsymbol{L}_1 - \boldsymbol{L}_0)]^{-1} \qquad (63)$$

In this equation, $\boldsymbol{I}$ is the identity tensor, $\boldsymbol{S}$ is the Eshelby tensor and $\boldsymbol{L_1}$ and $\boldsymbol{L_0}$ are the microscopic stiffness tensor for inclusion and resin, respectively.

Hence, substituting Equation (63) into Equation. (61) and can get the global concentration tensor $\boldsymbol{A}^I$ as

$$\boldsymbol{A}^I = [\boldsymbol{I} + \boldsymbol{S}:(\boldsymbol{L_0})^{-1}:(\boldsymbol{L_1} - \boldsymbol{L_0})]^{-1}:[c_0\boldsymbol{a}^0 + c_1\boldsymbol{a}^1 + c_1\boldsymbol{H}^1\boldsymbol{L_1}\boldsymbol{a}^I]^{-1} \qquad (64)$$

In this process, introduce J_2 flow rule to determine whether matrix is elastic or plastic, while CNT inclusion is assumed always being elastic because of great effective properties. And in elastic or plastic situation, hardening scalar r, accumulated plastic strain p, ductile damage D, micro stress $\boldsymbol{\sigma}$ and micro plastic strain $\boldsymbol{\varepsilon^p}$ are updated respectively.

The flow rule function is provided as follows.

$$f = \sigma_e^{trial} - 3G\Delta p - R(r) - \sigma_{y0} \qquad (65)$$

Where $R(r) = kr^m$ nonlinear isotropic hardening function is described by the scalar variable r. And k and m in the hardening function are material properties and σ_{y0} in the equation is the yield stress and $\sigma_e^{\text{trial}}$is the equivalent trial stress.

The equivalent trial stress is defined as

$$\hat{\sigma}_e^{trial} = L^{el}:\left[(\varepsilon_n + \Delta\varepsilon) - \varepsilon_n^p\right] \qquad (66)$$

The subscript e means equivalence of stress which follow the equation.

$$\sigma_e = J_2(\hat{\sigma}) = \left[\frac{3}{2}(\hat{s}):(\hat{s})\right]^{\frac{1}{2}} \tag{67}$$

In the equation, s is deviatoric stress which can be calculated by

$$\hat{s} = \hat{\sigma} - \frac{1}{3}(tr\hat{\sigma})1 \tag{68}$$

To deal with multivariate Newton's Iteration, first is to note several relationships.

The flow rule can also be expressed as

$$f_{\hat{\sigma}} \equiv \hat{\sigma}_e - \hat{\sigma}_e^{trial} + 3G\Delta p \tag{69}$$

All the stress and strain variable with $(\hat{\cdot})$ means accounting in the revolution of ductile damage which specifically represents.

$$(\hat{\cdot}) = \frac{(\cdot)}{1-D} \tag{70}$$

The basic of flow rule is to simulate material is in the state of elastic or plastic. Follow the Equation (65) can judge the state by

$$\begin{cases} elastic, f \le 0 \\ plastic, f > 0 \end{cases} \tag{71}$$

If $f \le 0$, it means that the prediction is correct, so

$$\hat{\boldsymbol{\sigma}}_{n+1} = \hat{\boldsymbol{\sigma}}_{n+1}^{trial} \tag{72}$$
$$\left(r_{n+1}, p_{n+1}, D_{n+1}, \varepsilon_{n+1}^p\right) = \left(r_n, p_n, D_n, \varepsilon_n^p\right)$$

On the other hand, if $f > 0$, which represents the equivalent trial stress $\hat{\sigma}_e^{trial}$ is larger than the sum of yield stress and hardening stress, and the assumption is incorrect that means plasticity occurs and it is necessary to find a $\hat{\boldsymbol{\sigma}}_{n+1}$ which can make $f = 0$. This process is called plastic corrector.

Since the relationship of

$$\hat{\boldsymbol{\sigma}}_{n+1} = \hat{\boldsymbol{\sigma}}_{n+1}^{trial} - \boldsymbol{L}^{el}:\Delta\boldsymbol{\varepsilon}^p \tag{73}$$

And because of the $\Delta\boldsymbol{\varepsilon}^{\boldsymbol{p}}$ is deviatoric, the Equation (73) becomes.

$$\hat{\boldsymbol{\sigma}}_{n+1} = \hat{\boldsymbol{\sigma}}_{n+1}^{trial} - 2\mathrm{G}\Delta\boldsymbol{\varepsilon}^p \tag{74}$$

Now the problem becomes to solve the unknown $\Delta\boldsymbol{\varepsilon}^p$. And introduce the vector N, which is normal to flow rule f.

$$N \equiv \frac{\partial f}{\partial \boldsymbol{\sigma}} = \left(\frac{3}{2}\right)\frac{s}{J_2(\boldsymbol{\sigma})} \tag{75}$$

Then simply find Δp instead of $\Delta\boldsymbol{\varepsilon}^p$ since

$$\Delta\boldsymbol{\varepsilon}^{p} = N\Delta\boldsymbol{p} \tag{76}$$

In previous section, the updated micro stress $\hat{\boldsymbol{\sigma}}_{n+1}$ have been derived. Then it is able to calculate effective stiffness of ductile matrix $\hat{\boldsymbol{L}}^{alg}$ at $n+1$ iteration

$$\delta\hat{\boldsymbol{\sigma}}_{n+1} = \hat{\boldsymbol{L}}^{alg}\delta\hat{\boldsymbol{\varepsilon}}_{n+1} \tag{77}$$

Where

$$C^{alg} = C^{ep} - (2G)^{2}\frac{\Delta p}{[1+(\frac{3}{2})g]}\frac{\partial^{2} f}{\partial\sigma\partial\sigma} \tag{78}$$

$$\hat{\boldsymbol{L}}^{alg} = \hat{\boldsymbol{L}}^{ep} - (2G)^{2}\frac{\Delta\boldsymbol{p}}{\left[1+\left(\frac{3}{2}\right)g\right]}\frac{\partial^{2} f}{\partial\hat{\boldsymbol{\sigma}}\partial\hat{\boldsymbol{\sigma}}}$$

$$\hat{\boldsymbol{L}}^{\boldsymbol{ep}} = \boldsymbol{L}^{\boldsymbol{el}} - (2G)^{2}\frac{\hat{\boldsymbol{N}}\otimes\hat{\boldsymbol{N}}}{h}$$

$$h = 3G + \frac{\partial R}{\partial r}$$

$$g = \frac{2G\Delta\boldsymbol{p}}{\hat{\boldsymbol{\sigma}}} > 0$$

$$\frac{\partial^{2} f}{\partial\hat{\boldsymbol{\sigma}}\partial\hat{\boldsymbol{\sigma}}} = \frac{1}{\hat{\sigma}_{e}}\left(\frac{3}{2}\boldsymbol{I}^{\boldsymbol{dev}} - \hat{N}\otimes\hat{\boldsymbol{N}}\right)$$

And then can get the local stiffness tensor as

$$\boldsymbol{L}^{\boldsymbol{alg}} = (1-D)\hat{\boldsymbol{L}}^{\boldsymbol{alg}} \tag{79}$$

It is noted that, mid-point rule at $n+\alpha$ is introduced to improve the accuracy. We use effective stiffness at $n+1$ and new calculated deriving $\hat{\boldsymbol{L}}^{alg}_{n+\alpha}$ as figure shown.

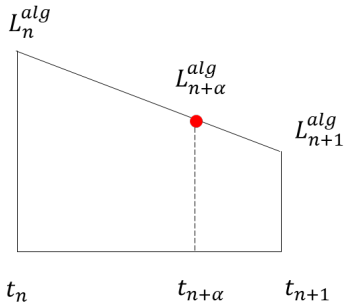

Figure 5. Scheme of Mid-Point Rule

$$\boldsymbol{L}^{alg}_{n+\alpha} = (1-\alpha)\boldsymbol{L}^{alg}_{n} + \alpha\boldsymbol{L}^{alg}_{n+1} \tag{80}$$

The equation is shown for both inclusion and matrix when calculating algorithmic tangent operator.

It is more complicated to consider the situation of damage comparing with no ductile damage case at the same time. It is need to satisfy three equations instead of one and to update three unknown variables in the meantime.

$$\begin{cases} f_{\hat{\sigma}} \equiv \hat{\sigma}_e - \hat{\sigma}_e^{trial} + 3G\Delta p = 0 \\ f_f \equiv J_2(\hat{\boldsymbol{\sigma}}) - R(r) - \sigma_{y0} = 0 \\ f_D \equiv \Delta D - y(\hat{\boldsymbol{\sigma}})\frac{\Delta r}{1-D} \end{cases} \tag{81}$$

In the equation, $y(\hat{\boldsymbol{\sigma}})$ is shorten notation which is related to strain energy release Y.

$$y = \left(\frac{Y}{S_0}\right)^s \tag{82}$$

$$Y = \frac{1}{2E}\left(\frac{\hat{\sigma}_e}{1-D}\right)^2 R_v$$

$$R_v = \frac{2}{3}(1+v) + 3(1-2v)\left(\frac{\hat{\sigma}_H}{\hat{\sigma}_e}\right)^2$$

$$\hat{\sigma}_H = \frac{\hat{\sigma}_{kk}}{3}$$

Where s is a material property and here is set to be 0.5.

Set the unknown variables are $\begin{Bmatrix} \Delta\hat{\boldsymbol{\sigma}} \\ \Delta r \\ \Delta D \end{Bmatrix}$. Following Newton's iteration

$$x_{i+1} = x_i - \frac{f(x_i)}{\frac{\partial f}{\partial x}} \tag{83}$$

So, for multivariate Newton's iteration, derive a Jacobian matrix.

$$\begin{Bmatrix} \Delta\hat{\boldsymbol{\sigma}} \\ \Delta r \\ \Delta D \end{Bmatrix}^{(k+1)} = \begin{Bmatrix} \Delta\hat{\boldsymbol{\sigma}} \\ \Delta r \\ \Delta D \end{Bmatrix}^{(k)} - \begin{bmatrix} \boldsymbol{I} + 2G\frac{\partial N^{tr}}{\partial\hat{\boldsymbol{\sigma}}}\Delta\boldsymbol{p}^{(k)} & \frac{2GN^{tr}}{1-D_n} & \frac{2GN^{tr}}{1-D_n}\Delta\boldsymbol{p}^{(k)} \\ (N^{tr})^T & -\left(\frac{\partial R}{\partial r}\right)^{(k)} - \frac{3G}{1-D_n} & \frac{3G\Delta\boldsymbol{p}^{(k)}}{1-D_n} \\ -\Delta\boldsymbol{p}^{(k)}\left(\frac{\partial y}{\partial\hat{\sigma}}\right)^{(k)^T} & -\frac{y^{(k)}}{1-D_n} & 1 - \frac{y^{(k)}\Delta\boldsymbol{p}^{(k)}}{1-D_n} \end{bmatrix} \begin{Bmatrix} f_{\hat{\sigma}} \\ f_r \\ f_D \end{Bmatrix}^{(k)} \tag{84}$$

$$\Delta p^{(k+1)} = \frac{\Delta r^{(k+1)}}{1-D_n}$$

In the equation, the partial derivative is calculated by.

$$\frac{\partial N^{tr}}{\partial \hat{\boldsymbol{\sigma}}} = \frac{1}{J_2(\hat{\sigma}'^{tr})}\left(\frac{3}{2}\boldsymbol{I} - \hat{\boldsymbol{N}} \otimes \hat{\boldsymbol{N}}\right) \tag{85}$$

$$\frac{\partial R}{\partial r} = hm(r)^{m-1}$$

$$\frac{\partial y}{\partial \hat{\sigma}} = \frac{\partial y}{\partial \hat{\sigma}_{ij}} = \frac{\partial y}{\partial \hat{\sigma}'_{ij}} = \frac{s}{S_0^s}\left[\frac{(1+\nu)\hat{\sigma}'_{ij}\hat{\sigma}'_{ij}}{2E(1-D_n)^2} + \frac{(1-2\nu)\hat{\sigma}_{pp}}{6E(1-D_n)^2}\right]^{s-1}\left[\frac{(1+\nu)\hat{\sigma}'_{ij}}{E(1-D_n)^2} + \frac{(1-2\nu)\hat{\sigma}_{pp}\delta_{ij}}{3E(1-D_n)^2}\right]^{s-1}$$

The main scheme is depicted as Figure 6 shown. From known n iteration stress $\hat{\boldsymbol{\sigma}}_n$, first assuming trial stress $\hat{\boldsymbol{\sigma}}_n^{trial}$, and then through Newton iteration, internal iteration is adopted to find a new stress which is close to real value.

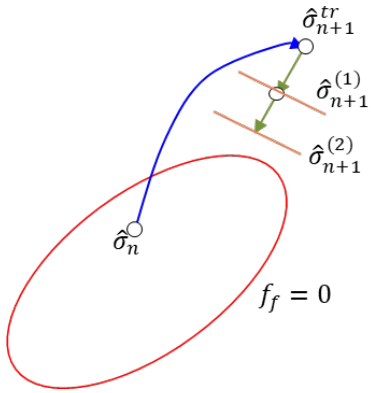

Figure 6. Return Mapping Algorithm

It is noted that the fully implicit Newton Raphson's iteration is operated in the t_n to t_{n+1} time domain, so when updating global concentration tensor $\boldsymbol{A}^I$, in the outer iteration, Newton Raphson's iteration will still in the time domain $[t_n, t_{n+1}]$

Hence, from Equation (83), it is capable to solve Newton's iteration and get.

$$\hat{\boldsymbol{\sigma}}_{\boldsymbol{n+1}} = \hat{\boldsymbol{\sigma}}_{\boldsymbol{n}} + \boldsymbol{\Delta}\hat{\boldsymbol{\sigma}}^{(\boldsymbol{k+1})} \tag{86}$$

$$r_{n+1} = r_n + \Delta r^{(k+1)}$$

$$D_{n+1} = D_n + \Delta D^{(k+1)}$$

$$\Delta\, p^{(k+1)} = \frac{\Delta r^{(k+1)}}{1 - D_n}$$

The overall Newton iteration is shown as

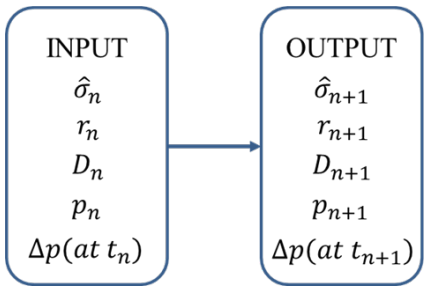

Figure 7. In & Output of Newton Raphson's Iteration

After Newton Raphson's iteration, the updated $\hat{\boldsymbol{\sigma}}, r, D$ and Δp Satisfy the three equations in Equation (81)

Figure 8 shows the convergent condition of fully implicit Newton Raphson's iteration. The iteration convergent quickly in first several iterations which indicates the Newton iteration is working well.

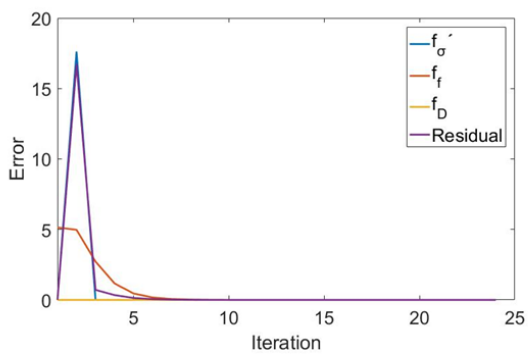

Figure 8. Convergent of multivariable Newton Iteration

To evaluate plasticity, first use scale transition techniques, from macro to micro, and achieve constitutive properties of matrix and inclusion respectively. a macro stress increment and initial identity strain concentration tensor $\boldsymbol{A}^I$ are initialized.

Then it is able to get micro strain increment with Equation (87), for inclusion and matrix respectively.

$$\Delta\boldsymbol{\varepsilon}^I = \boldsymbol{A}^I_{old} : \Delta\boldsymbol{E} \tag{87}$$

$$\Delta\boldsymbol{\varepsilon}^0 = \frac{\Delta\boldsymbol{E} - c_1\Delta\boldsymbol{\varepsilon}^I}{1 - c_1}$$

In the equation, superscript I and 0 means inclusion and matrix phase respectively. $\Delta\boldsymbol{E}$ is macro strain increment which can be set in advance. And c_1 is volume fraction of inclusion.

And then can calculate stress increment in microscale

$$\boldsymbol{\sigma} = (1 - D)\boldsymbol{L}^{el}\colon(\boldsymbol{\varepsilon} - \boldsymbol{\varepsilon}^{p}) \tag{88}$$

Where D is variable which describes ductile damage. D=0 represents no damage in matrix. In the equation, ε is microscale strain, ε^{p} is micro plastic strain and $\boldsymbol{L}^{el}$ is elastic stiffness of material.

It is noted that $D = \frac{A_D}{A_0}$, where A_D and A_0 are the area of damage and the total area respectively.

Also, relationship between r, p and D is shown as.

$$\dot{r} = (1 - D)\dot{p} \tag{89}$$

Where r is hardening function scalar and p is accumulated plastic strain.

Then following section 2.4.2, the updated stress and get algorithm tangent operator for inclusion and matrix respectively are calculated.

After get effective stiffness $\hat{\boldsymbol{L}}_{n+\alpha}^{alg}$ for fiber and matrix, in the microscale, it is able to get strain concentration tensor with interfacial damage as Equation (54) shows. And based on Equation (63) the macroscale concentration tensor $\boldsymbol{A}^{I}$ can be derived from

$$\boldsymbol{A}^{I} = \boldsymbol{a}^{I}\colon\boldsymbol{A}^{0} \tag{90}$$

Here, subscript I and 0 indicate inclusion and matrix phase respectively, and lowercase a means local microscale strain concentration tensor and capital $\boldsymbol{A}$ is global strain concentration tensor. Where $\boldsymbol{A}^{0}$ is, and $\boldsymbol{L_1}$ is effective stiffness calculated from Equation (91).

$$\boldsymbol{A}^{0} = (c_0\boldsymbol{I} + c_1\boldsymbol{a}^{I} + c_1\boldsymbol{H}^{1}\colon\boldsymbol{L}_1\colon\boldsymbol{a}^{I})^{-1} \tag{91}$$

After getting new $\boldsymbol{A}^{I}$, it is need to check the residual which is.

$$\boldsymbol{R} = \boldsymbol{A}^{I}\colon\Delta\boldsymbol{E} - \Delta\boldsymbol{\varepsilon}^{I} \tag{92}$$

If the residual is, continue to the Mori-Tanaka homogenization and finally derive macro strain from

$$\Delta\boldsymbol{\Sigma} = \boldsymbol{L}^{MT}\colon\Delta\boldsymbol{E} \tag{93}$$

Otherwise, $\boldsymbol{A^I}$ is need to be update and repeat the simulation from Equation (87).

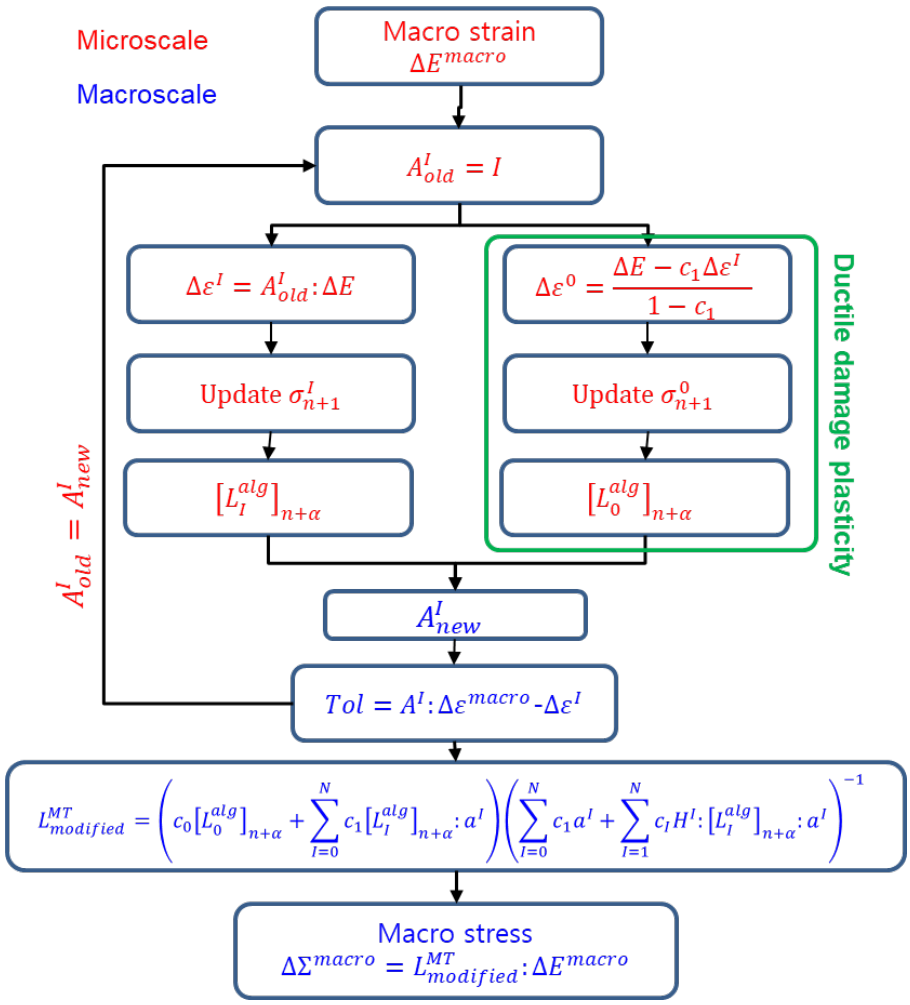

Figure 9. Scheme of micromechanics Mori-Tanaka model

The whole scheme is shown as Figure 9.

2.5. Comparison of LS homogenization and Mori-Tanaka Homogenization

Mori-Tanaka homogenization and Lippmann-Schwinger homogenization are two commonly used methods for multiscale analysis of composite materials. Although both methods aim to provide effective solutions for predicting the macroscopic properties of composites

from their underlying microstructures, they employ different theoretical frameworks and mathematical techniques.

Mori-Tanaka homogenization is a self-consistent method that employs a perturbation technique to derive an effective medium approximation (EMA) for the composite material. The method assumes that the local field inside the composite material can be approximated by a series of homogeneous EMA fields that capture the interaction between the constituent phases. This approach allows for the computation of effective properties such as the elastic modulus and Poisson's ratio, which can be used to predict the macroscopic behavior of the composite. Mori-Tanaka homogenization is computationally efficient and has been shown to yield accurate results for a wide range of composite materials[98].

On the other hand, Lippmann-Schwinger homogenization is a rigorous method based on the theory of scattering in physics. The method represents the composite material as a collection of randomly oriented and distributed inclusions and considers the interaction between the inclusions and the surrounding matrix material. The resulting interaction problem is solved using the Lippmann-Schwinger equation, which relates the macroscopic properties of the composite to the scattering properties of the constituent phases. Lippmann-Schwinger homogenization is computationally intensive and requires the solution of a large system of equations, but it has been shown to provide accurate results for complex composite materials with highly irregular microstructures. Moreover, cluster-based Lippmann-Schwinger homogenization provides an improved simulation model to obtain the efficiency and accuracy. As shown in Figure 10, Lippmann Schwinger homogenization based on actual coordinates or voxel, and will calculate voxel by voxel. The Mori-Tanaka homogenization[72] can simulation the composites RVE with each material phases.

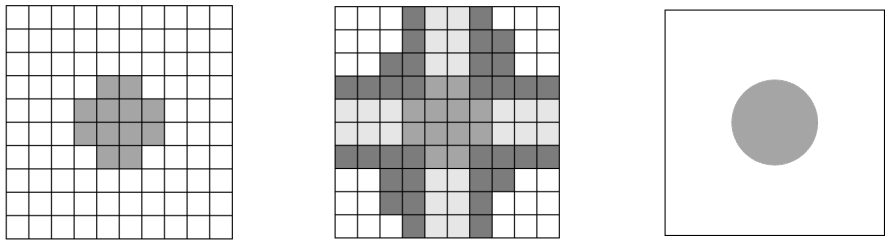

Figure 10. 2D Fiber reinforced composites RVE with (a). Lippmann Schwinger homogenization, (b). cluster-based Lippmann Schwinger homogenization, (c). Mori-Tanaka homogenization

In summary, both Mori-Tanaka homogenization and Lippmann-Schwinger homogenization are valuable tools for multiscale analysis of composite materials, but they employ different theoretical frameworks and mathematical techniques. Mori-Tanaka homogenization is a perturbation-based method that is computationally efficient and widely used, while Lippmann-Schwinger homogenization is a rigorous method based on the theory of scattering that provides accurate results for complex microstructures at the cost of greater computational expense. Moreover, cluster-based Lippmann-Schwinger homogenization provides satisfied efficiency and accuracy with known cluster distribution.

In a two-phase fiber-reinforced composites model, both the cluster-based Lippmann-Schwinger homogenization and Mori-Tanaka homogenization methods share the same kinematic integral, as depicted in Figure 11. However, the key difference lies in the iteration process.

In the cluster-based Lippmann-Schwinger homogenization method, the strain increment is iteratively computed within each of the N clusters, ranging from 1 to N. The macroscale strain is then determined by volume averaging the strain contributions from each cluster. This iterative process allows for a more accurate estimation of the macroscale behavior by considering the local effects within individual clusters.

On the other hand, in the Mori-Tanaka homogenization method, both local and global strain concentrations are utilized to calculate the micro- and macro-scale models. The homogenization is performed by considering the strain contributions from each phase. This approach incorporates the influence of the individual phases on the overall behavior of the composite.

These different iteration procedures in the two homogenization methods reflect their respective strategies for capturing the heterogeneous nature of the composites. While the cluster-based Lippmann-Schwinger homogenization focuses on local cluster effects and volume averaging, the Mori-Tanaka homogenization accounts for strain concentrations at both micro- and macro-scale levels, considering the distinct contributions of the composite phases.

By employing these distinct iteration approaches, both methods aim to provide an accurate representation of the composites' mechanical behavior, enabling the prediction of their overall response based on the characteristics of their constituent phases.

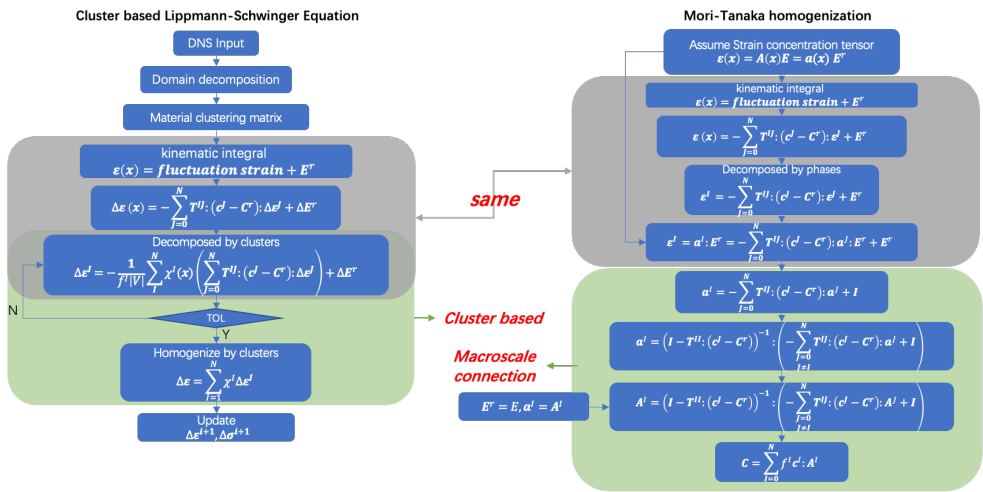

Figure 11. Flowchart of Homogenization Methods

On the other hand, there are notable differences in the input and output of the two homogenization methods as shown in Figure 12. While both methods require input parameters such as the constituent matrix properties and volume fraction of each material, there are distinct considerations for each method.

In cluster-based Lippmann-Schwinger homogenization, which is a computational method, the first step involves discretizing the RVE of the fiber-reinforced composites. The cluster information, which can be obtained through direct numerical simulation (DNS) or finite element simulations, serves as input data. This information characterizes the local behavior of the clusters within the RVE. The homogenization process then calculates stress and strain increments, which are volumetrically averaged by the clusters. This approach provides a means to determine the local and averaged behavior of the composite material.

On the contrary, Mori-Tanaka homogenization requires additional consideration of the aspect ratio of the inclusion phases within the composite. This aspect ratio plays a role in the calculation of the Eshelby tensor, which is utilized to capture the influence of the inclusion's shape on the simulation results. The Eshelby tensor has a direct impact on the determination of the composite's constitutive matrix, influencing the overall behavior of the material.

Consequently, the output of the cluster-based Lippmann-Schwinger homogenization method consists of stress and strain increments, volumetrically averaged by the clusters. This output provides insights into the local and cluster-level mechanical response of the composite. On the other hand, Mori-Tanaka homogenization yields a global constitutive matrix that characterizes the macroscopic behavior of the composite material. This matrix encapsulates the composite's overall response, considering the influence of the inclusion phases and their respective aspect ratios.

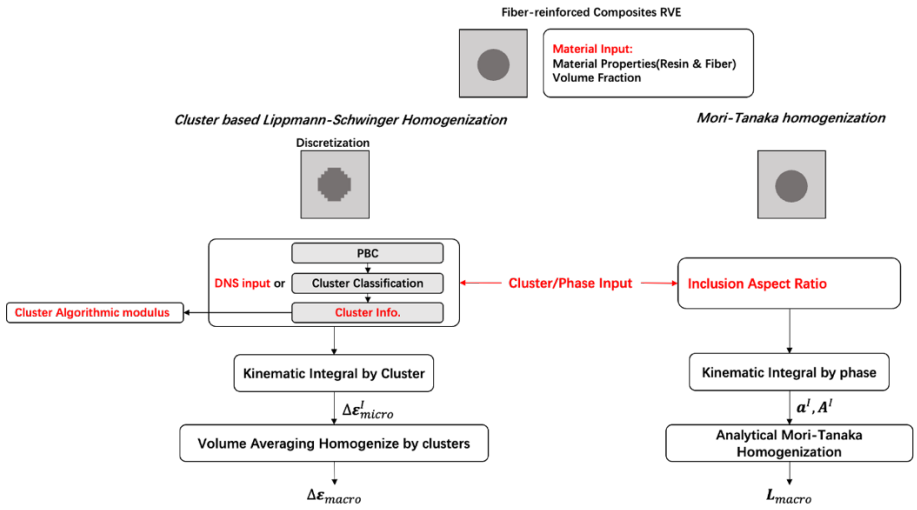

Figure 12. Input & Output Comparison of Homogenization Methods

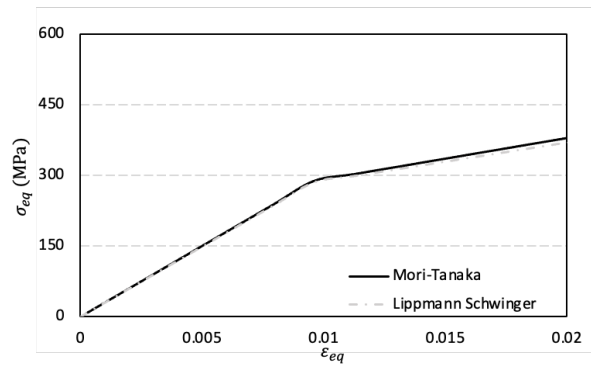

Figure 13. Comparison of stress and strain curve of fiber reinforced composites

Figure 16 presents a comparison between Lippmann-Schwinger homogenization and Mori-Tanaka homogenization for a simple example of straight fiber-reinforced composites. The material properties used in this comparison are provided in Table 2. The results demonstrate that the differences between the two homogenization methods are minimal, indicating the validity and accuracy of both models.

While the presented homogenization methods exhibit favorable performance for this specific example, it is important to acknowledge their limitations. Classical analytical homogenization approaches may face challenges when dealing with complex geometric structures, as

they rely on simplifying assumptions that may not accurately capture the intricacies of the material behavior. On the other hand, computational homogenization methods can be computationally demanding and time-consuming due to the need for extensive numerical calculations.

To address these limitations, the thesis incorporates improved versions of both analytical and computational homogenization techniques. These enhanced approaches aim to overcome the drawbacks of classical methods and leverage the advantages offered by computational homogenization, while reducing the computational burden. By adopting these improved methods, the thesis explores the benefits of analytical and computational homogenization for a wide range of composite materials with complex geometric structures.

Through the utilization of these advanced homogenization techniques, the thesis aims to provide a comprehensive understanding of the mechanical behavior of composite materials, considering their intricate geometries. By combining the advantages of analytical and computational approaches, the thesis contributes to the development of more accurate and efficient methods for analyzing and predicting the behavior of complex composite materials.

Chapter 3. Multiscale Homogenization for SCA composites

3.1. Multistep Analytical Homogenization

As part of the investigation into the mechanical behavior of Sheet Molding Compound (SMC) composites, the impact of multi-step homogenization on the development of a hierarchical micromechanics model is presented. The research focused on the compression molding process, whereby fiber chips are dispersed heterogeneously in the SMC composites with overlapping. It is important to note that the extent of overlapping between fiber chips can have a significant effect on the mechanical properties of the composites.

To address this issue, a multi-step homogenization method is proposed which can accurately replicate the mesostructured morphology of these composites with computational efficiency. It is believed that this method holds promise for a range of real-world applications in the field of composite materials.

The approach involves three distinct homogenization steps. The first of these steps involves modeling individual fiber chips as wavy fibers, which are known to closely resemble the actual shape of the chips. Next, a unit SMC layer that comprises the randomly oriented fiber chips and resin is modeled. Finally, a third homogenization step based on the Rule of Mixtures (ROM) is performed, which enables to estimate the effective properties of the final SMC composite. This step is crucial because it allows to determine the overall strength and durability of the composite.

Overall, the multi-step homogenization method proposed holds significant promise for the development of hierarchical micromechanics models in the field of composite materials. By modeling the

mesostructured morphology of SMC composites with computational efficiency, it is aimed to improve the accuracy of mechanical property predictions, paving the way for more robust and reliable composite materials in the future.

3.1.1 1st Homogenization

The thesis describes the initial homogenization models of a chip with wavy fibers through the one-site MT method. To express the wavy fibers, the projection length of the fiber on the x-axis is designated, allowing for the generation of z-coordinate values along the x-axis. This results in the wavy fiber adopting an arbitrary shape on the x-z plane.

In Figure 14, it is observed that the representation of three wavy fibers with six equidistant x-coordinate values and arbitrary z-coordinate values. The waviness in the fibers is controlled by the standard deviation of a preset normal distribution. By randomly sampling from this distribution, the fibers' z-coordinate values are determined. An increase in standard deviation results in a more random waviness pattern. For the straight fiber, the standard deviation is set to zero.

To summarize, the essay presents a systematic approach for modeling wavy fibers in chips using the OS MT method. The inclusion of figures further enhances the reader's understanding of the concept.

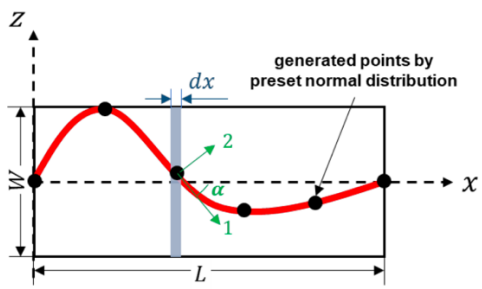

Figure 14. Representation of random fiber waviness

The schematic illustration presented in Figure 14 depicts a fiber arrangement where the fiber is positioned on the x-z plane, with L and W denoting the fiber's length and width, respectively. The fiber exhibits a wavy pattern described by a polynomial mathematical function, represented by $z(x) = ax^3 + bx^2 + cx + d$. To obtain the coefficients of the function, a curve-fitting approach is employed. To determine the gradient along the x-axis, an analytical differentiation technique is employed, allowing for the precise determination of the gradient along the wavy fiber.

From the global to local coordinates system, the stress and strain tensors are converted through a rotational transformation tensor $[T_{ij}]$, as follows.

$$\begin{bmatrix}\sigma_{xx}\\ \sigma_{yy}\\ \sigma_{zz}\\ \tau_{yz}\\ \tau_{xz}\\ \tau_{xy}\end{bmatrix} = [T_{ij}]^{-1}\begin{bmatrix}\sigma_{11}\\ \sigma_{22}\\ \sigma_{33}\\ \tau_{23}\\ \tau_{13}\\ \tau_{12}\end{bmatrix}, \begin{bmatrix}\varepsilon_{xx}\\ \varepsilon_{yy}\\ \varepsilon_{zz}\\ \gamma_{yz}\\ \gamma_{xz}\\ \gamma_{xy}\end{bmatrix} = [T_{ij}]^{-1}\begin{bmatrix}\varepsilon_{11}\\ \varepsilon_{22}\\ \varepsilon_{33}\\ \gamma_{23}\\ \gamma_{13}\\ \gamma_{12}\end{bmatrix} \tag{94}$$

Where $[T_{ij}]$ is defined by fiber angle α as shown in Figure 14 and expressed as.

$$T_{ij} = \begin{bmatrix} m^2 & 0 & n^2 & 0 & 2mn & 0 \\ 0 & 1 & 0 & 0 & 0 & 0 \\ n^2 & 0 & m^2 & 0 & -2mn & 0 \\ 0 & 0 & 0 & m & 0 & -n \\ -mn & 0 & mn & 0 & m^2 - n^2 & 0 \\ 0 & 0 & 0 & n & 0 & m \end{bmatrix} \tag{95}$$

Where $m = \cos\alpha\,, n = \sin\alpha$

As shown in Figure 14, the angle α is determined by the derivative of $z(x)$. Using the line integral with $[T_{ij}]$, the stiffness matrix in the global coordinates system can be transformed to the local coordinates system as follows.

$$\boldsymbol{L}_{chip}^{wavy} = \frac{1}{L}\int_0^L T_{ij}^{-1}\boldsymbol{L}_{chip}^{straight}T_{ij}dx \tag{96}$$

which can also be denoted as $\boldsymbol{L}_{chip}^{straight}$. Finally, the stiffness of a single wavy fiber chip is obtained through the rotational

transformation expressed in Equation (96). Figure 15 illustrates the modeling procedures of the fiber chip.

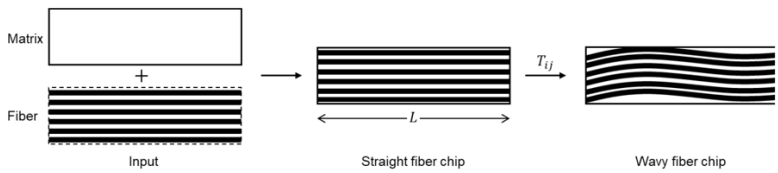

Figure 15. The micromechanics modeling of wavy fiber chip

3.1.2 2nd Homogenization

Subsequently, the second phase of Mori-Tanaka modeling and homogenization is conducted by embedding fiber chips with the desired orientation into the Sheet Molding Compound (SMC) layer. In traditional Mori-Tanaka homogenization, the fiber chips are oriented in the x-axis direction of the global coordinate system. However, in the case of SMC composites fabricated through compression molding, the fiber chips may possess non-uniform orientation. Consequently, each SMC layer consists of fiber chips with non-uniform orientation. The influence of this non-uniform orientation on the composite's effective properties is assessed using an orientation averaging tensor, which was originally proposed by Odegard et al.[17]

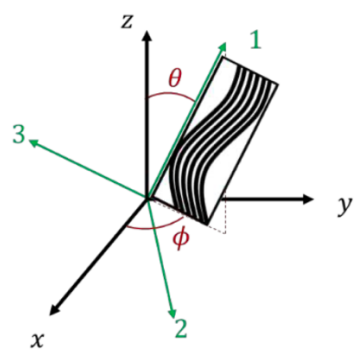

Figure 16. Defining the angles of fiber chips' orientation

The stiffness tensor with the direction of the SMC layer is mathematically expressed in Equation (97).

$$\boldsymbol{L}^{layer} = (c^0\boldsymbol{L}^0 + \sum_{I=1}^{N} c^I\langle \boldsymbol{L}^I : \boldsymbol{a}^I\rangle) : (c^0\langle \boldsymbol{a}^0\rangle + \sum_{I=1}^{N} c^I\langle \boldsymbol{a}^I\rangle)^{-1} \quad (97)$$

In this equation, the inclusion stiffness ($\boldsymbol{L}^I$) is replaced into $\boldsymbol{L}_{chip}^{wavy}$ in Section 3.1.1. The fiber chips are considered inclusions in the second homogenization for the SMC layer modeling. The notation $\langle\ \rangle$ represents the orientation-averaging tensor computed by Equation (98), as follows

$$\langle X\rangle_{ijkl} = \frac{\int_0^{\frac{\pi}{2}}\int_{-\pi}^{\pi} X'_{ijkl}(\phi,\theta)\lambda(\theta)\sin\theta d\phi d\theta}{\int_0^{\frac{\pi}{2}}\int_{-\pi}^{\pi}\lambda(\theta)\sin\theta d\phi d\theta} \quad (98)$$

where $\lambda(\theta)$ is the function of θ. X'_{ijkl} is the transformed tensor from the local to global coordinate systems. X'_{ijkl} is defined in Equation (99)

$$X'_{ijkl} = t_{ip}t_{jq}t_{kr}t_{ls}X_{pqrs} \quad (99)$$

Where $\boldsymbol{t} = \begin{bmatrix} cos\theta & -\sin\theta & 0 \\ \sin\theta\cos\phi & \cos\theta\cos\phi & -\sin\phi \\ \sin\theta\sin\phi & \cos\theta\sin\phi & \cos\phi \end{bmatrix}$, and the angle θ and ϕ are defined as shown in Figure 16.

To express the random orientation of the fiber chips, $\lambda(\theta)$ is assumed to follow Equation (100)

$$\lambda(\theta) = e^{-k\theta^2} \quad (100)$$

As k decreases to zero, the fiber chips are randomly oriented. On the other hand, when the k diverges to an infinite value, fiber chips become aligned in the x-axis direction. Thus, the fiber chips' orientation changes with $\lambda(\theta)$. The manufacturing process naturally makes randomly distributed fiber chips.

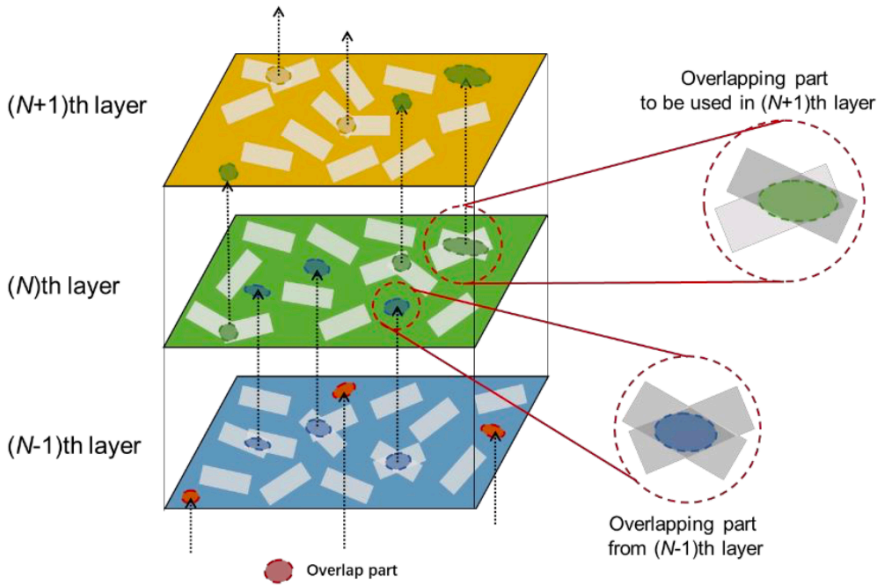

Figure 17. Overlapping parts of chips and mapping to the upper layer

The orientation of fiber chips and the overlapping phenomenon arise due to the high-volume fraction during the compression molding process. In Figure 17, the SMC layer is set to a depth of one unit, leading to the presence of overlapping parts from the lower layer in the current layer.

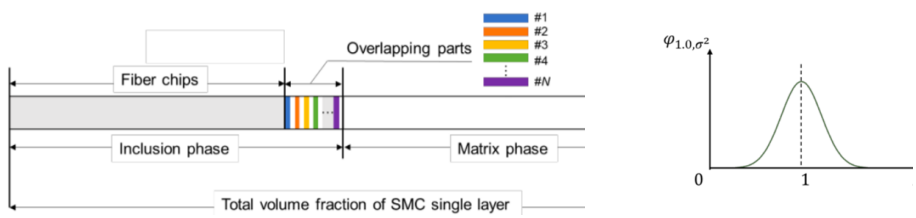

(a) (b)

Figure 18. (a) The contents of SMC composites (b) the normal distribution in terms of aspect ratio (AR) for overlapping parts

In this study, the overlapping parts are considered as individual ellipsoidal inclusions, and their shape is determined based on their diameter and aspect ratio. As shown in Figure 18(a), numerous overlapping parts exist due to the high-volume fraction of the SMC composites. To model the overlapping parts with arbitrary sizes, a micromechanics model is utilized. Since the shape of overlapping parts

is unpredictable, their aspect ratio is assumed to follow a normal distribution, as shown in Figure 18(b). The SMC layer modeling incorporates the multi-site (MS) Mori-Tanaka model since the overlapping parts are regarded as ellipsoidal inclusions with varying sizes.

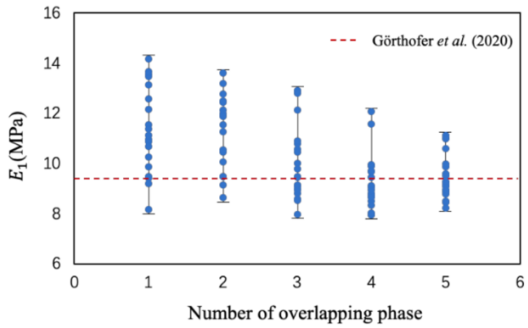

Figure 19. Effect of the number of overlapping phases on the effective elastic modulus

To conduct the MS Mori-Tanaka (MT) modeling, a suitable volume fraction of overlapping phases needs to be determined. In this study, 20 trials were conducted with a 10% overlapping volume fraction of the MS-MT model to compute the elastic modulus. The parameters used in Section 3.1.2 were employed for all 20 trial simulations. The obtained results were then compared with those of Görthofer et al.[105]. As depicted in Figure 19, insufficient overlapping phases lead to a slightly higher calculated modulus value than that reported in the literature. Additionally, the variance of modulus tends to converge gradually as the number of overlapping phases increases. However, a large number of phases results in excessive computational time. Therefore, considering both computational efficiency and validity, the number of overlapping phases is set to five.

3.1.3 3rd Homogenization

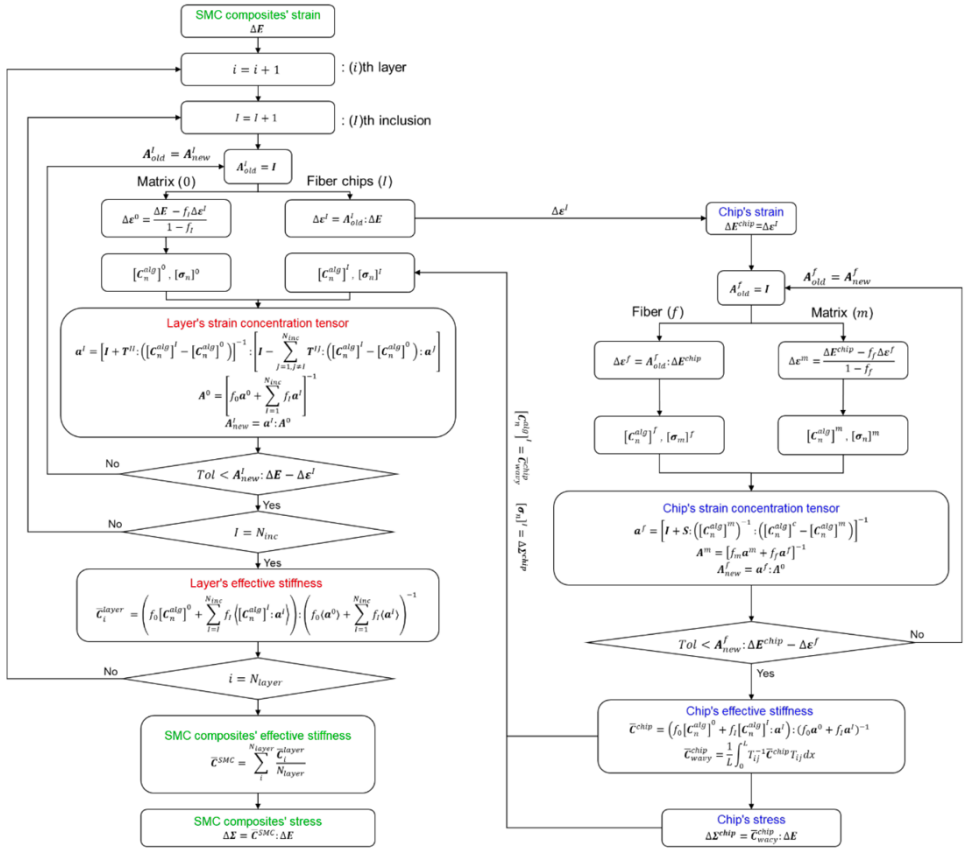

Figure 20. Flowchart of multi-step homogenization

Finally, the effective properties of the SMC composites are obtained through the Rule of the mixtures (ROM) with virtual layer-by-layer laminations. The homogenized unit SMC layers are laminated into an SMC solid composite. Depending on the preset variables, SMC layers have different homogenized properties calculated in the second homogenization. The effective stiffness of SMC composites is expressed with the homogenized unit layers' stiffnesses, as follows.

$$\boldsymbol{L}_{SMC} = \sum_{i=1}^{N_{layer}} \frac{\boldsymbol{L}_{ilayer}}{N_{layer}} \tag{101}$$

Where N_{layer} is the total number of layers. In Equation (101), because the layers constituting the SMC composite are assumed to

have the same thickness, the volume fraction of each layer is $1/N_{layer}$.

As a result, the average value of layers' effective stiffness is the effective stiffness of the SMC composites.

The multi-step homogenization approach for SMC composites is presented in Figure 20. This approach employs the OS and MS models of the Mori-Tanaka (MT) method for the fiber chip and SMC layer, respectively. Subsequently, the Rule of Mixtures (ROM) is utilized to determine the effective stiffness of SMC composites. The algorithm initiates from the strain increment of SMC composites, which is partitioned into the matrix and fiber chip phases. Additionally, the strain of the fiber chips is further divided into the matrix and fiber phases. The first homogenization is carried out based on the material properties of the matrix and fiber, and the effective stiffness and stress of the fiber chip with wavy fibers are transferred to the second homogenization. The orientation averaging tensor is utilized to determine the effective stiffness of the SMC layer due to the non-uniformly distributed fiber chips. In the second homogenization step, ellipsoidal inclusions are assumed to represent overlapping parts. The final step involves using ROM to obtain the effective stiffness of SMC composites. The simulations at each stage are executed concurrently, with the ductile damage plasticity of the matrix being applied to the matrix phase. The input to this algorithm is the strain increment of SMC composites, while the output is the stress increment of SMC composites, which is calculated through the multi-step homogenization.

3.2. Multiscale cluster based SCA homogenization

A fiber-reinforced FE microscale model is presented to indicate the domain decomposition process.

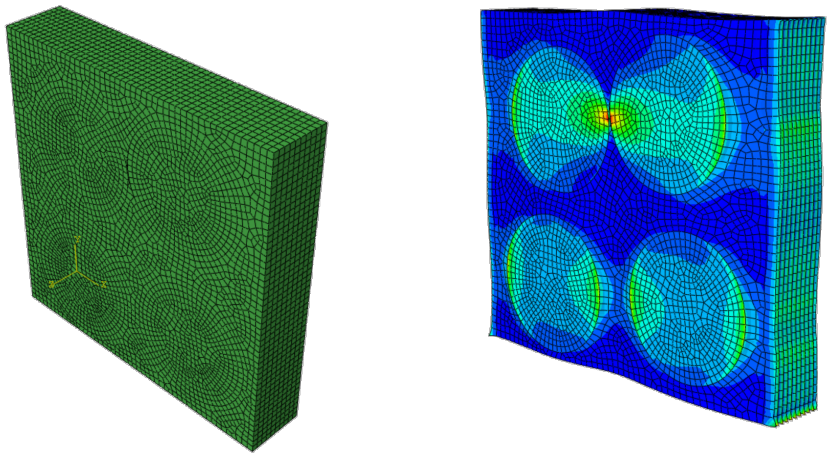

(a) (b)

Figure 21. (a) FE model for fiber-reinforced composites (b) Fiber-reinforced composites model after PBC

As shown in Figure 21, micromechanical FE model of fiber-reinforced composites before and under periodic boundary condition is presented.

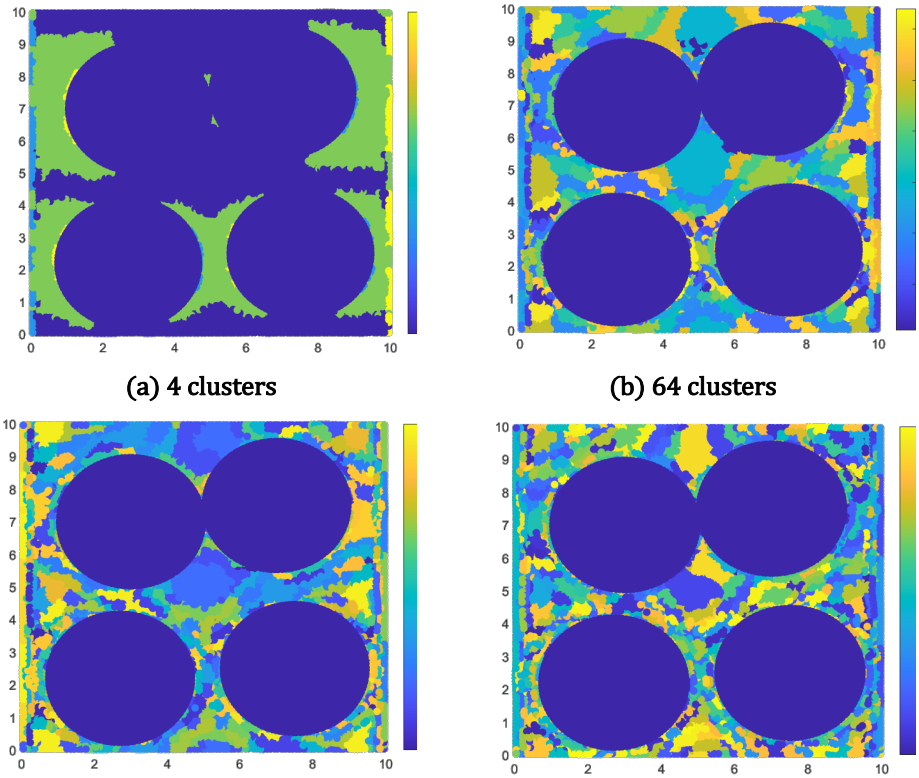

(a) 4 clusters (b) 64 clusters

(c) 128 clusters (d) 256 clusters

Figure 22. Cluster distribution of fiber-reinforced composites model with (a) 4 clusters (b) 64 clusters (c) 128 clusters (d) 256 clusters

Figure 22 presents a comparison between the cluster distribution obtained from FE calculation under periodic boundary condition and the proposed self-consistent clustering analysis with various number of clusters for matrix phase. This is expected, as the proposed approach aims to predict the global (homogenized) mechanical response as accurately as possible with the minimum amount of information necessary. To improve the resolution at these regions, the total number of clusters could be increased or, alternatively, a nonlinear mapping of the k-means clustering could be applied so that more clusters are assigned to regions requiring higher resolution. However, finding these regions remains an issue, as different loading conditions lead to different localization areas.

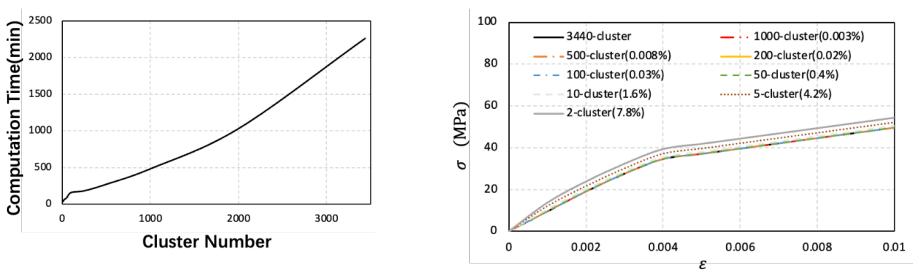

(a) (b)

Figure 23. The effect of number of clusters

Until now, the computational cost reduction achieved by the method has not been quantified. Despite the obvious reduction achieved in the number of degrees of freedom, the system of equations being solved uses an iterative approach, and each equation involves the summation over every cluster. Thus, there is a clear trade-off between the compression of information achieved by the clustering procedure and the actual solution of the Lippmann-Schwinger equations. Figure 23(a) illustrates a comparison of computation time between the proposed approach for different numbers of clusters and the DNS. The results are promising, particularly

considering that the DNS finite element analyses were performed using a commercial code that was significantly optimized, while the proposed method was implemented in MATLAB. The microscale and macroscale FE model is composed by 3440 and 32140 elements, respectively, and the computational time is almost proportional to the number of clusters in the system, indicating that the most time-consuming part is to update the internal variables locally at each cluster.

Towards the end of the curve in Figure 23(a), the analysis reveals that the largest number of clusters is 3440. This indicates that the multiscale model is still primarily based on individual elements. In the macroscale model, each element requires the reloading of the 3440-cluster microscale model, resulting in the updating of 3440*3440 interaction tensors. Consequently, this leads to a significant increase in computational calculations and a subsequent exponential growth in computation time.

The observed exponential growth in computation time highlights the computational challenges associated with the current approach. As the number of clusters increases, the computational demands become increasingly burdensome. Therefore, it is essential to explore strategies that can effectively mitigate the exponential increase in computation time and improve the efficiency of the multiscale model.

In Figure 23(b) the error is compared with the results of element based multiscale model, the number of cluster from 100 to 200 is appropriate for an efficient and accurate SMC composites modeling.

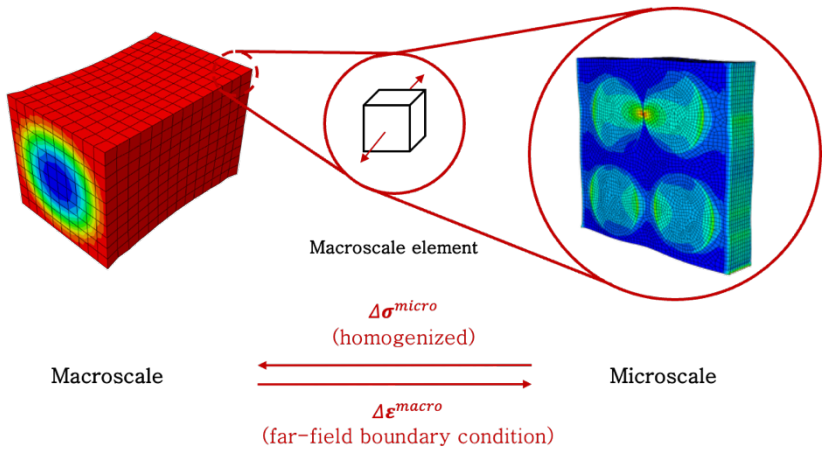

Figure 24. Multiscale model for fiber-reinforced composites

Figure 24 illustrates that the homogenized stress increment of the entire microscale model is intended to serve as the calculation result for the macroscale finite element model. Furthermore, the far-field strain loading of the macroscale model element is used for iterative calculation of the microscale model.

The thickness of microscale model is set to be small compare with the other dimensions because to simulate the random waviness of fibers in macroscale model.

1. Build microscale model in ABAQUS.
2. Run microscale model under periodic boundary condition and save data (Coordinates, strain concentration tensor) in ABAQUS.
3. Use k-means clustering method in MATLAB and save cluster information (cluster number for each element, volume fraction and strain concentration tensor for each cluster).
4. Build and run macroscale model in ABAQUS.

Figure 25. Process for multiscale fiber-reinforced composites simulation

As shown in Figure 25, the data from the microscale finite element model is stored in a .txt file using UMAT in ABAQUS. Prior to this, the microscale model is computed under periodic boundary conditions. The data obtained during this computation includes the coordinates of each Gauss point, as well as the strain concentration tensor derived from the stress and strain increments. The coordinate

information for each element is utilized to update the interaction tensor and the reference material matrix.

The data obtained from the microscale finite element model is saved in a .txt file using the UMAT in ABAQUS. This involves performing calculations under periodic boundary conditions and storing data such as coordinates for each Gauss point and the strain concentration tensor computed from stress and strain increments. The coordinate information for each element is then used to update the interaction tensor and reference material matrix.

Subsequently, the data is imported into MATLAB for k-means clustering simulation. This involves generating cluster numbers for each element, as well as volume fraction and strain concentration tensor for each cluster. These results are saved in a .txt file.

Next, a macroscale model is constructed and executed along with the data from steps 2 and 3, as illustrated in Figure 25. During the macroscale model execution, the microscale model runs concurrently in each element in the form of cluster simulation to obtain results.

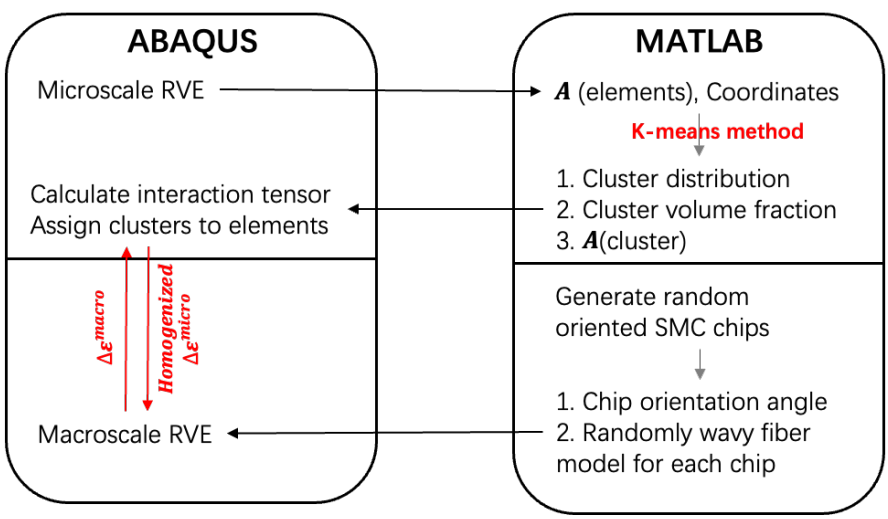

Figure 26. Data transform of multiscale SCA model for SMC

Figure 26 illustrates the data transformation process between the micro and macro scale models, as well as the data transfer between ABAQUS and MATLAB. At the microscale, the K-means method is employed to convert the element-based model into a cluster-based model. This transformation allows for efficient calculation by preserving the cluster information. At the macroscale, the orientation angles and the wavy fiber function are randomly generated and stored for finite element (FE) simulations. These generated parameters enable the simulation of realistic composites with randomly oriented fibers and wavy characteristics.

Chapter 4. Results

This Chapter presents the results obtained using two different homogenization methods, namely Lippmann-Schwinger homogenization, and Mori-Tanaka homogenization. Both methods are applicable to SMC composites and are used to investigate the mechanical response of the composite material.

4.1. Results of analytical homogenization

4.1.1 Effects of interfacial damage

Figure 27 shows a variation of effective Young's modulus with varying damage parameters α and β. Here in Figure 27, waviness w=0.1 and volume fraction of CNT is 0.1. The rate of changes of the stiffness was lessened as the damage parameters become larger. Also, it is noticed that the stiffness seems to be more sensitive to the normal damage (β) than the shear interfacial damage (α).

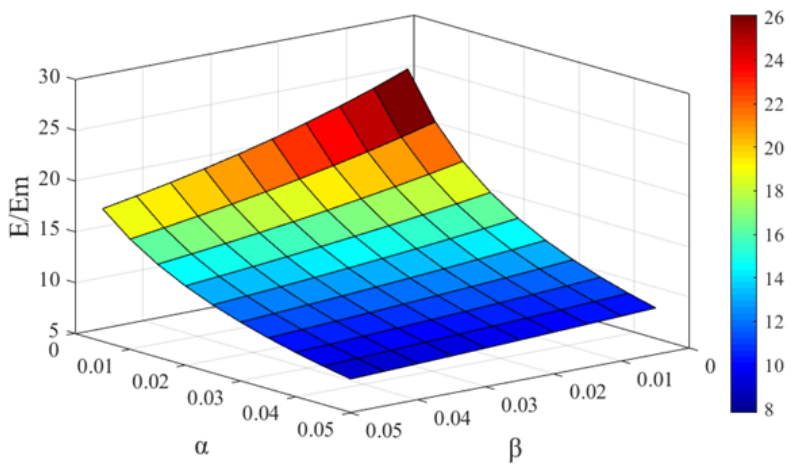

Figure 27. Effective properties with various interface damage

Figure 28 indicates the effective young's moduli (E_1 and E_3) of 3D aligned CNT nanocomposites as one of the aligned angles ϕ varies and the waviness changes. The other Euler angle Θ is fixed at 90 degrees. The waviness a=0.1 and volume fraction equals to 0.1. For damage case, α=0.1163 and β=0.0332. Young's modulus (E_1) in the longitudinal direction is sensitive to both the orientation and waviness, whereas young's modulus (E_3) in the transverse direction is insensitive to the orientation changes by the angle ϕ. Figure 28 shows damage parameter indeed having a negative effect on effective properties and the influence will become smaller when the damage parameter become larger.

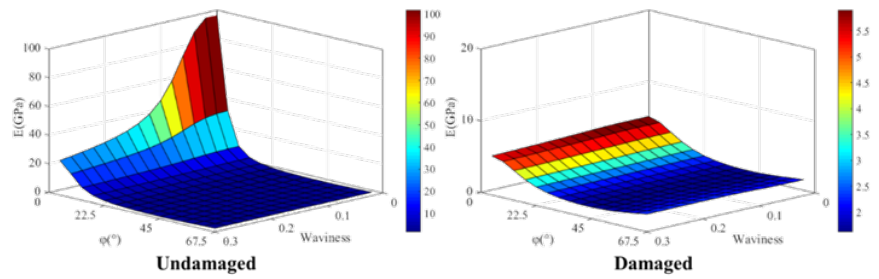

(a)

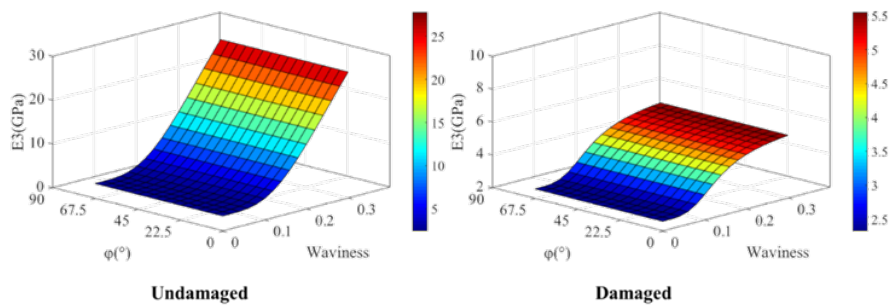

(b)

Figure 28. (a) Longitudinal and (b) transverse effective Young's modulus with varying orientation, waviness and damage parameter α and β

4.1.2 Effects of plasticity and ductile damage

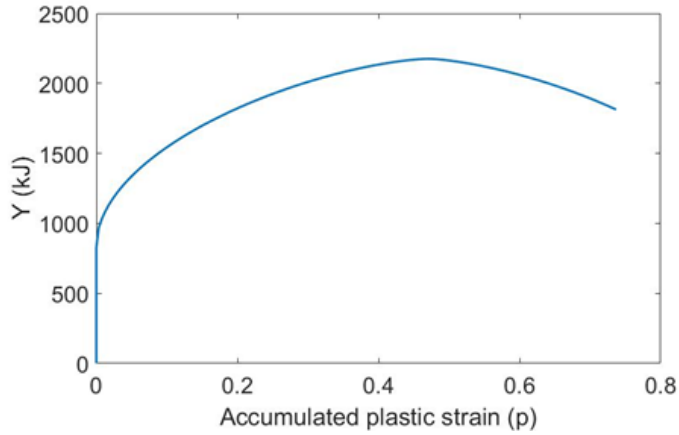

Figure 29. The effect of p on strain release energy Y

Figure 40 gives the relationship of accumulated plastic strain and strain energy release. From the very beginning of plastic occurrence, large amount of energy released, and the rate of increment become smaller with the evolution of p.

Material properties used in Figure 40 to Figure 35 are based on Table 1.

	Matrix	Inclusion
Young's Modulus	2GPa	1000GPa
Poisson Ratio	0.39	0.22
Yield stress	60.5MPa	-
Hardening Function	$h = 63MPa$ $m = 0.4$	-

Table 1. Material properties of plasticity simulation

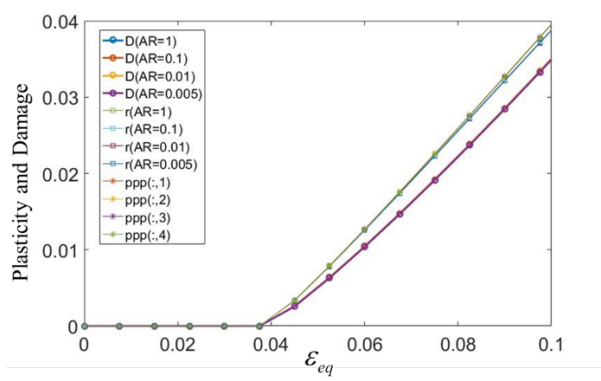

Figure 30. Plasticity and damage evolution with various aspect ratio

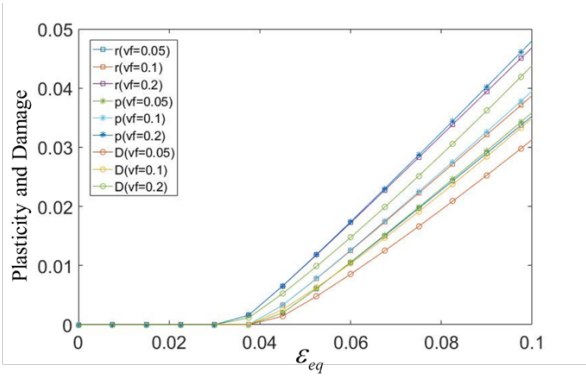

Figure 30. The influence of volume fraction on plastic and damage evolution

In the Figure 29, accumulated plastic strain, ductile damage, and hardening scalar have few relationships with aspect ratio which indicates the shape of inclusion has little influence on damage evolution. In the meanwhile, it is able to see ductile damage is smaller than p and r. In the case of without considering ductile damage, r and p are defined to have same value. And since, D is no larger than 1, and from Equation (89), p is slightly smaller than r.

On the other hand, presents that volume fraction affects damage revolution greatly. Still with the slight difference between p and r, damage and plastic strain will increase largely if volume fraction increases.

From Figure 31, it is found that volume fraction of inclusion not only effects the elastic range, but also plastic part. The slope of linear elastic curve shows effective performance of composites, also, the rate of stress increment increases with the increasing of volume fraction.

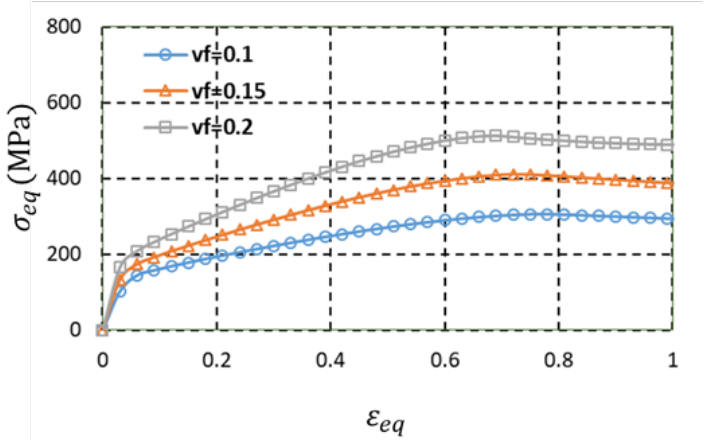

Figure 31. The effect of volume fraction

(Interfacial damage: α=0.3, β=0; Aspect Ratio: 0.01)

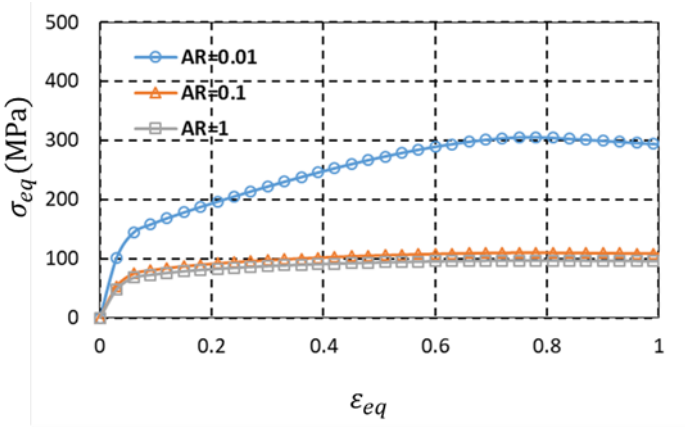

Figure 32. The effect of aspect ratio

(Interfacial damage: α=0.3, β=0; Aspect Ratio: 0.1)

Aspect ratio, as another factor which influences the stress-strain curve greatly. In the Figure 32, when aspect ratio increases, which means the shape of inclusion changes from a disk like plate to a sphere, effective properties reduce. It is also found that, from sphere shape inclusion to cylinder shape fiber, in another word, AR=∞, the effective properties will still decrease.

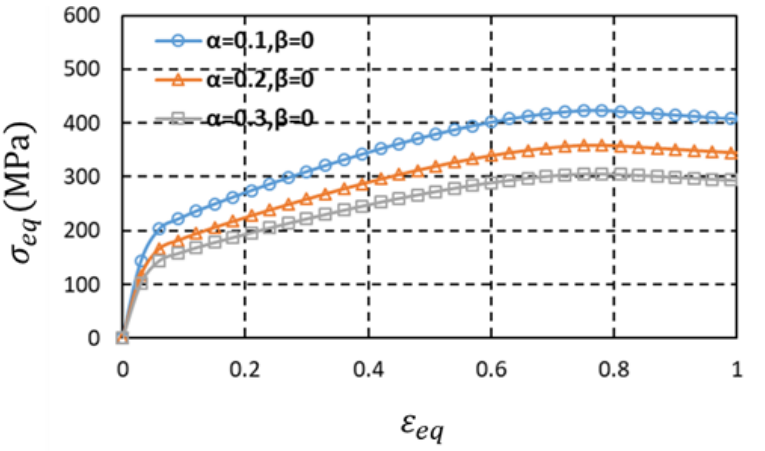

Figure 33. The effect of tangential damage

(Volume Fraction: 0.1; Aspect Ratio: 0.1)

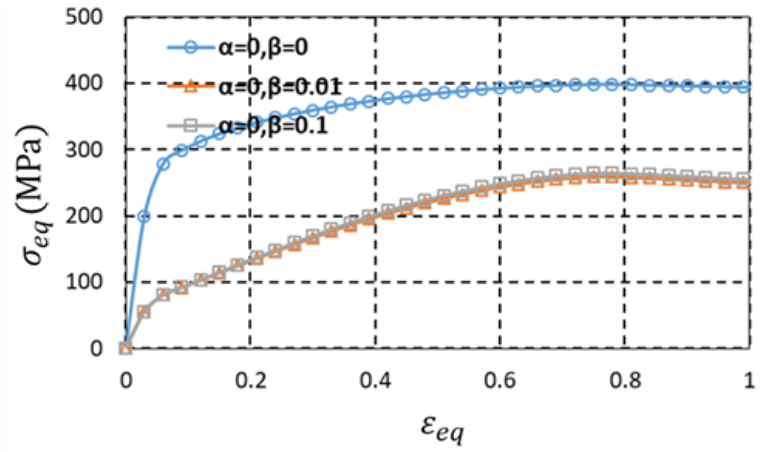

Figure 34. The effect of normal damage

(Volume Fraction: 0.1; Aspect Ratio: 0.01)

In Figure 33 and Figure 34, it mainly indicates how interfacial damage affect stress-strain curve. α, which means tangential damage have softer effect comparing with radial damage β. Curves in various tangential damage α shows similar tendency both in elastic part and plastic range, while β influences elastic range greatly.

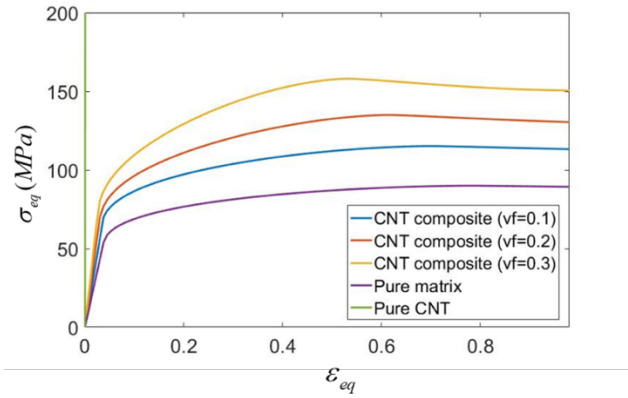

Figure 35. CNT nanocomposites elasto-plastic simulation

(Waviness: 0, α=0.3, β=0)

Figure 35 shows the plastic performance of CNT nanocomposites, to achieve cylinder shape CNT fiber model, set aspect ratio to be very large which is close to infinite. And compare the performance among pure CNT fiber, pure matrix and CNT nanocomposites with various volume fraction. The CNT fiber has significant mechanical properties which increase greatly. And CNT nanocomposites show better effective properties both in elastic and plastic range. Although every 10% of CNT inclusion will greatly improve the properties.

4.2. Results of multistep homogenization for SMC

4.2.1 Model Validation with literatures

The proposed hierarchical micromechanics model is validated with the results from the literature. Görthofer et al.[105] developed a rapid microstructure generator of SMC composites through closure approximations for the fiber orientation tensor. They utilized E-glass fiber and unsaturated polyester polyurethane hybrid (UPPH) resin for fiber chips. The material properties are summarized in Table 2.

	E-Glass Fiber	UPPH
Young's Modulus (GPa)	72	3.4
Shear Modulus (GPa)	29.51	1.23
Poisson Ratio	0.22	0.385

Table 2. Material parameters of fiber chips (Kehrer et al. 2018)

	Gorthofer et al.[105]	Pre-sented
E_L(GPa)	37.73	38.75
E_T(GPa)	10.33	10.61
G_L(GPa)	3.58	4.87
G_T(GPa)	3.64	4.87
v_L	0.477	0.489
v_T	0.292	0.318

Table 3. Results comparison of fiber chip

	Gorthofer et al.[105]	Trauth et al. [30]	Kehrer et al.[106]	Presented
E_x(GPa)	9.42	10.96±0.3	10.92±0.6	9.88±0.5
E_y(GPa)	8.21	9.25±1.0	8.28±0.5	7.46±0.6
E_z(GPa)	6.19			7.46±0.6
G_{yz}(GPa)	1.95			3.02±0.5
G_{xz}(GPa)	1.96			
G_{xy}(GPa)	3.11			3.43±0.4
v_{yz}	0.398			0.398±0.1
v_{xz}	0.368			0.385±0.1
v_{xy}	0.342			0.385±0.1

Table 4. Comparison of effective elastic properties of SMC composites for the proposed method and literatures

The authors utilized numerical full-field homogenization to evaluate the elastic properties of SMC composites. The fiber volume

fraction within each fiber chip was set to 50%. The resulting elastic properties in the longitudinal and transverse directions are summarized in Table 3, which are consistent with the literature.

To evaluate the elastic properties of SMC composites, the authors compared their proposed model with Görthofer et al.[105] SMC model that used fiber chips. In the literature model, the fiber chips had a size of 50 mm × 5 mm and were distributed in a 250 mm × 250 mm plate with seven layers. The orientation tensor was determined through μ-CT scans and image processing, and the resulting effective orthotropic engineering properties are presented in Table 4.

In the proposed model, the authors distributed fiber chips in a matrix with an orientation variable k=0.32, assuming 20 layers with a 50% volume fraction of chips in each layer. To incorporate the effects of waviness and orientation, the authors set the number of overlapping types to five, including six types of inclusions, including SMC chips, with a 10% volume ratio in the total fiber volume. The resulting material properties were obtained through ten trials with the randomness of waviness (std=1), and the proposed method was compared with experiments and literature. The comparison results demonstrate the validity of the proposed method with high accuracy, although slight differences may be attributed to waviness and orientation effects that cannot coincide precisely with the experiments and the literature.

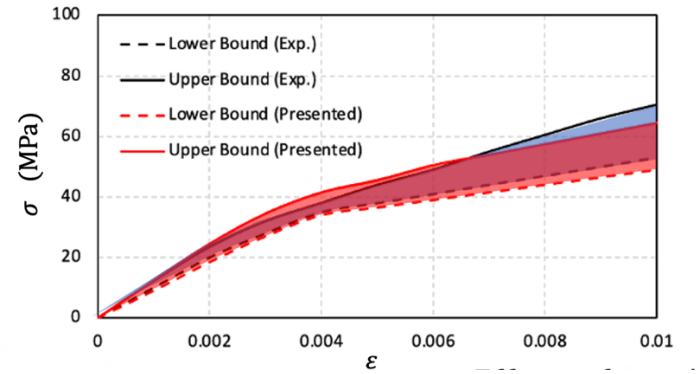

Figure 36. Comparison of multistep homogenization for SMC

In Figure 36, the experiment data[107] encompasses a comprehensive set of 20 tests conducted on SMC specimens subjected to tensile loading.

The upper and lower bounds of experiments data are from the randomness of density differences because of hollows, diameters of fibers, orientation of SMC chips and other geometrical features during the manufacturing process of SMC.

The upper and lower bounds of experimental data are attributed to the inherent randomness arising from various factors in the manufacturing process of SMC composites. These factors include the presence of hollows, variations in fiber diameters, orientations of SMC chips, and other geometric features.

During the manufacturing process, the random distribution of these features introduces inherent variability in the resulting composite material. This variability manifests as deviations in the mechanical properties, such as density differences, observed in the experimental data. The upper and lower bounds represent the extreme values within this range of variability.

The presented results of multistep homogenization, obtained through an extensive series of 50 simulations, showcase the range of mechanical properties exhibited by the material. Notably, the performance of the SMC in both the elastic and plastic regions demonstrates remarkable characteristics, thereby substantiating its validation and efficacy.

4.2.2 Effect of overlapping

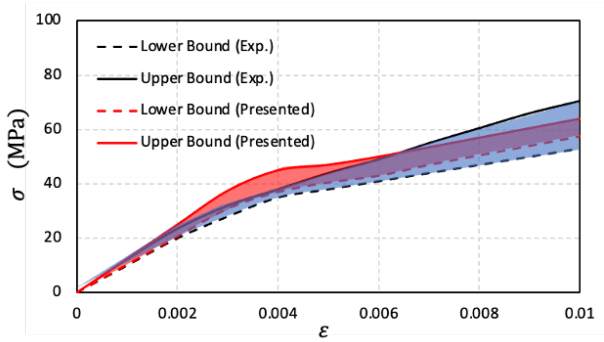

Figure 37. Effect of overlapping parts

In Figure 37, the experimental data comprising 20 tensile tests are sourced from Jekabsons et al. [107]. The highlighted range denoted by red signifies the range of overlapping inclusions employed in the experimental setup, ranging from 5% to 10%, as discussed in section 3.1. The upper bounds results obtained from the presented model assume the absence of any overlapping inclusions within each layer of the SMC. However, as the level of overlapping increases, the model's results exhibit a closer proximity to the corresponding experimental data.

4.2.3 Effect of waviness and orientation

The mechanical properties of SMC composites are significantly influenced by the waviness of fibers and the orientation of chips, which are dependent on the manufacturing process. In this section, a case study is conducted to investigate the effect of fiber waviness on the mechanical behavior of SMC composites. The micromechanical model assumes the material properties of constituents presented in Table 2, and monotonic loading is applied in the longitudinal direction. Wavy fibers are categorized into three cases, and their stress-strain responses are summarized in Figure 38(a), indicating a reduction in mechanical properties due to the presence of waviness.

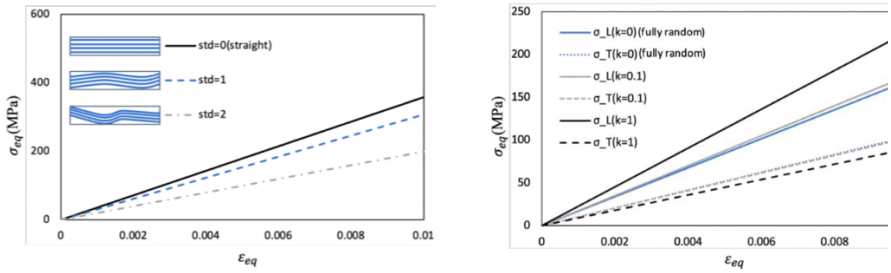

(a) (b)

Figure 38. The stress-strain curves (a) the influence of the waviness on SMC chip and (b) the influence of the orientation on SMC composites

Figure 39. The change of chip orientation with an increment of k

Furthermore, the effect of orientation is studied by increasing the orientation variable k, and the longitudinal and transverse stress-strain responses of the SMC composites are plotted in Figure 39(b). The degree of anisotropy of the composites is expressed by $\lambda(\theta)$, which is a function of k. The schematic tendency of anisotropy is depicted in Figure 40, where the longitudinal behavior becomes stiffer as fiber chips are aligned with the loading direction, while the elastic behavior along the x and y directions becomes similar for randomly distributed chips. The parametric study highlights the significance of waviness and orientation as critical parameters in determining the elastic behavior of both fiber chips and SMC composites. Finally, the nonlinear behavior of SMC composites under cyclic loading is evaluated.

4.2.4 The SMC micromechanics model under cyclic loading

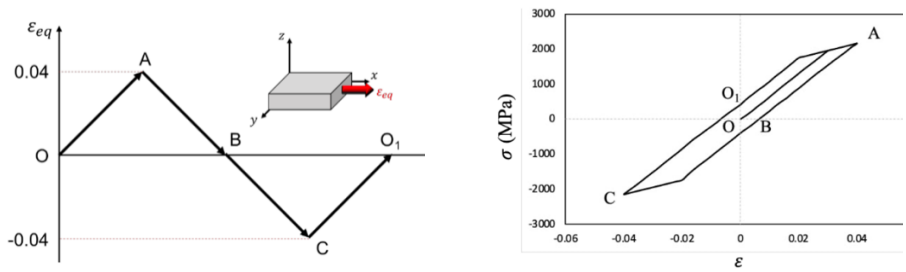

(a) (b)

Figure 40. Periodic boundary condition application in ABAQUS

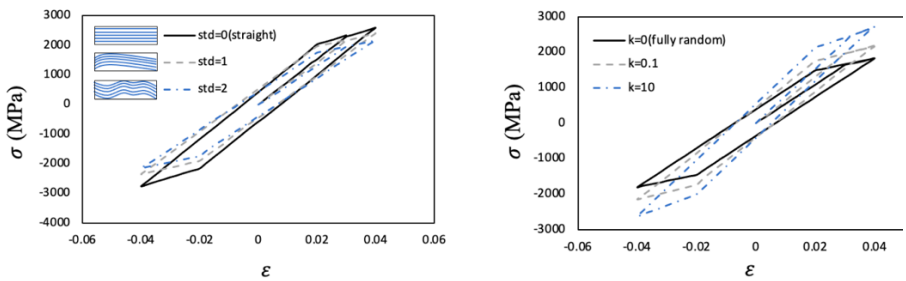

(a) (b)

Figure 41. Cyclic stress-strain responses (a) waviness (b) orientation distribution

Ascertaining the nonlinear behavior of Sheet Molding Compound (SMC) composites under cyclic loading is critical for the design and optimization of the material. In this section, a hierarchical micromechanics model is employed to investigate the effect of waviness on the cyclic stress-strain behavior of SMC composites. The cyclic loading condition is applied to the x-axis in the interval [-0.04, 0.04], as shown in Figure 41, with the amplitude of strain selected such that it leads to plasticity and nonlinear behavior.

During the loading process, as strain incrementally increases, ductile damage and plasticity emerge. Once the strain reaches the maximum positive loading point A, the loading strain linearly decreases to the negative maximum loading point C. The response of SMC composites follows elastic behavior until reaching the plastic

regime. After this point, a hardening slope with ductile damage is observed, leading to the generation of unrecoverable plastic strain in the compressive loading. In this study, CF/PA6 SMC composites are modeled using material parameters reported in the literature [108, 109].

Figure 41(a) presents the impact of waviness on the cyclic stress-strain responses of SMC composites. The material properties are adopted from Table 2, with the fiber volume fraction and orientation variable k set at 20% and 0.1, respectively. The calculation generates fiber chips with three different waviness patterns, and the results show that waviness negatively affects both elastic and damage-plastic regimes. Additionally, Figure 41(b) illustrates that the random distribution of fiber chips with k=0 leads to a decline in material properties in both the elastic and damage plastic regimes. All models considered in this study include wavy fibers in the fiber chips with a standard deviation of 2. Notably, the aligned fibers in the loading direction provide higher elastic and plastic properties, whereas the randomly distributed fiber chips decrease the performance of SMC composites along the loading direction.

Overall, the results emphasize the importance of considering the waviness and orientation of fibers in predicting the nonlinear behavior of SMC composites under cyclic loading.

4.3. Results of multiscale cluster based SCA simulation

4.3.1 Validation of multiscale cluster based SCA simulation

	Fiber	Matrix
Young's Modulus (GPa)	230	3.9
Poisson Ratio	0.27	0.39

Table 5. Material parameters of fiber and matrix

The validation of the proposed SCA multiscale model was carried out by comparing the results with those reported in the literature. The study utilized fiber and matrix resin, with material properties summarized in Table 5. The results obtained from the proposed model were found to be in good agreement with those reported in Mori-Tanaka, demonstrating the validity and accuracy of the proposed approach.

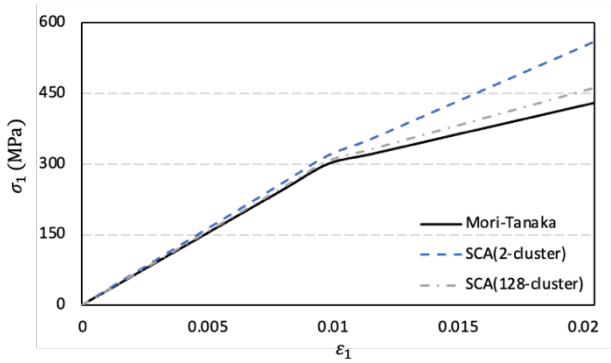

Figure 42. Comparison of various homogenization methods

The data presented in Figure 42, which has been obtained using the Mori-Tanaka homogenization method described in Chapter 3, demonstrate that the yield strength of the matrix material is 29MPa, while the hardening slope is 100MPa. It is noteworthy that the elastic and plastic regions exhibit a similar trend with little difference, suggesting that the multiscale SCA composites model has been successfully validated.

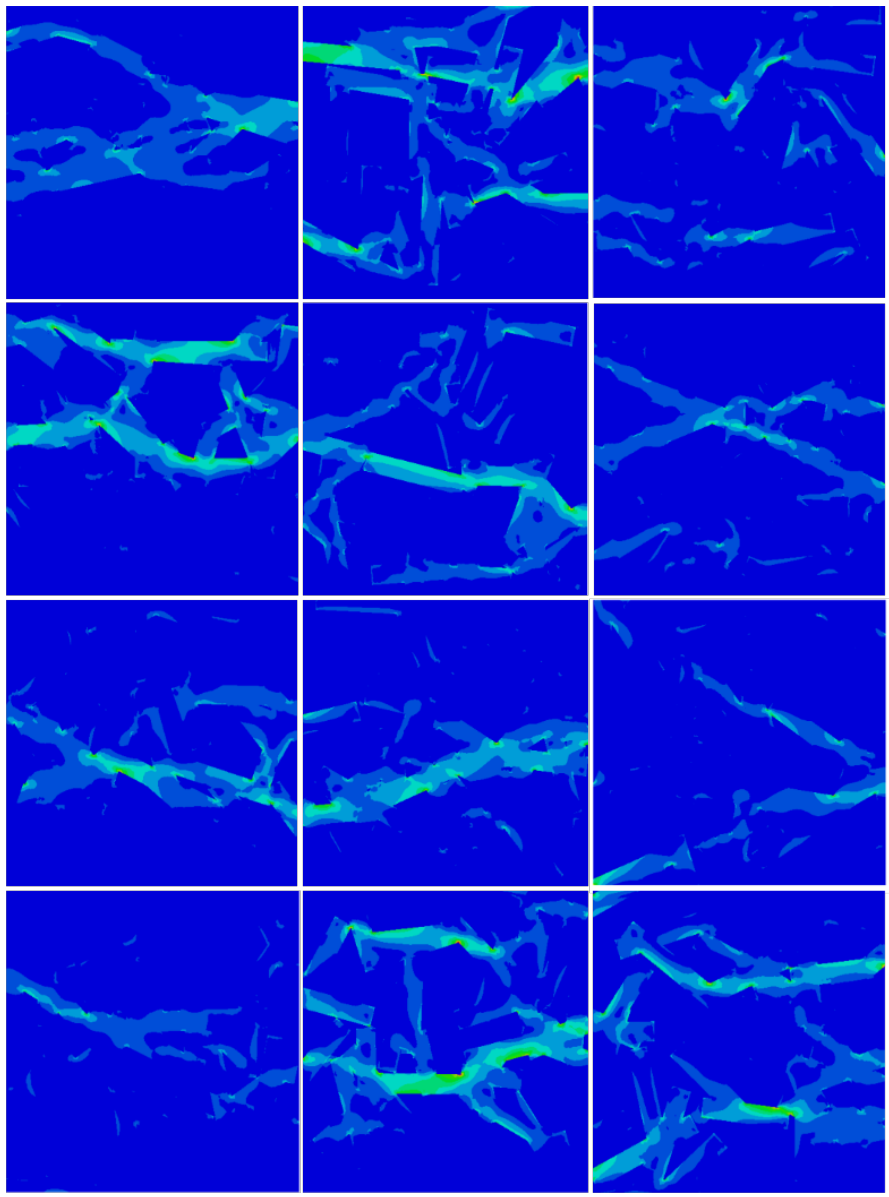

(a)

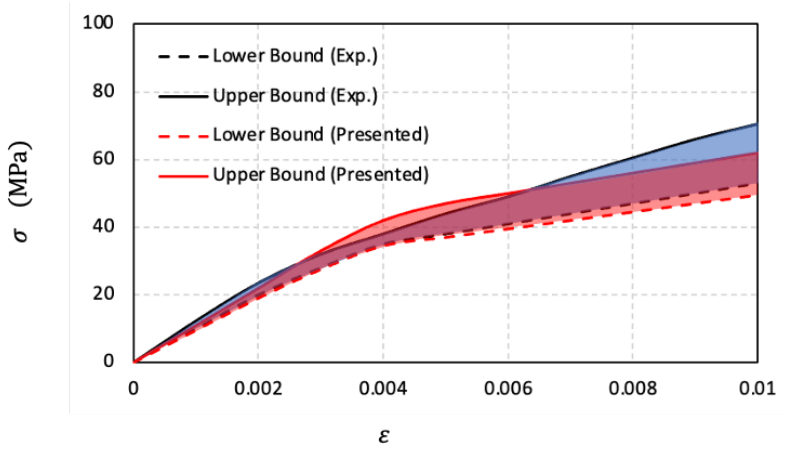

(b)

Figure 43. Validation of random orientation

Figure 43 (a) showcases a collection of 12 contours representing randomly generated SMC composites. The macroscale model utilized in the cluster-based SCA simulation incorporates a total of 20 instances of randomly oriented SMC chips. Correspondingly, the experiment data employed for comparative analysis consists of 20 sets of tensile tests[107]. It is worth noting that the ranges of the experiment data and the proposed model in Figure 43(b) exhibit a substantial degree of overlap. This overlap strongly suggests the validation of the multiscale cluster-based model and its ability to accurately capture the mechanical behavior of the SMC composites.

4.3.2 The effect of waviness and orientation

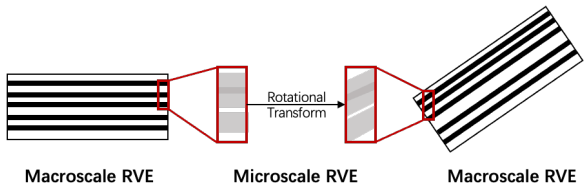

Figure 44. Rotate transformation of multiscale SCA model

The mechanical properties of SMC composites are strongly influenced by various factors, including the waviness of fibers and the orientation of chips, which are dependent on the manufacturing

process. In this study, the impact of fiber waviness on the mechanical behavior of SMC composites was comprehensively investigated through rotational transformation in Sections 5.3.

To incorporate the effect of waviness and fiber chip orientation in the microscale analysis of SMC composites, the rotation angle is stored in the element of the macroscale model, which is then used in the computation of the microscale representative volume element (RVE), as illustrated in Figure 44.

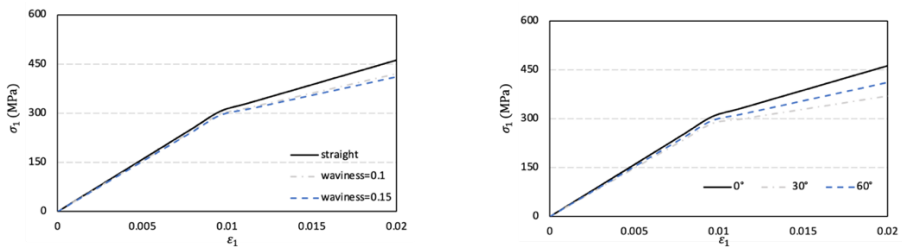

(a) (b)

Figure 45. The effect of (a) waviness and (b) orientation

The impact of waviness and fiber orientation on the mechanical properties of SMC composites is a critical aspect of their overall performance. The results of the macroscale and microscale models presented in Figure 45, as shown in Figure 24, demonstrate the influence of these factors. The presence of waviness and fiber orientation significantly reduces the mechanical properties of the composite material in the longitudinal direction. These findings highlight the importance of carefully controlling the manufacturing process to minimize the effects of waviness and orientation and ensure optimal mechanical performance in SMC composites. As such, these results provide valuable insights for engineers and researchers seeking to improve the design and development of these advanced composite materials.

4.3.3 The comparison of multiscale SCA simulation and multistep homogenization of SMC

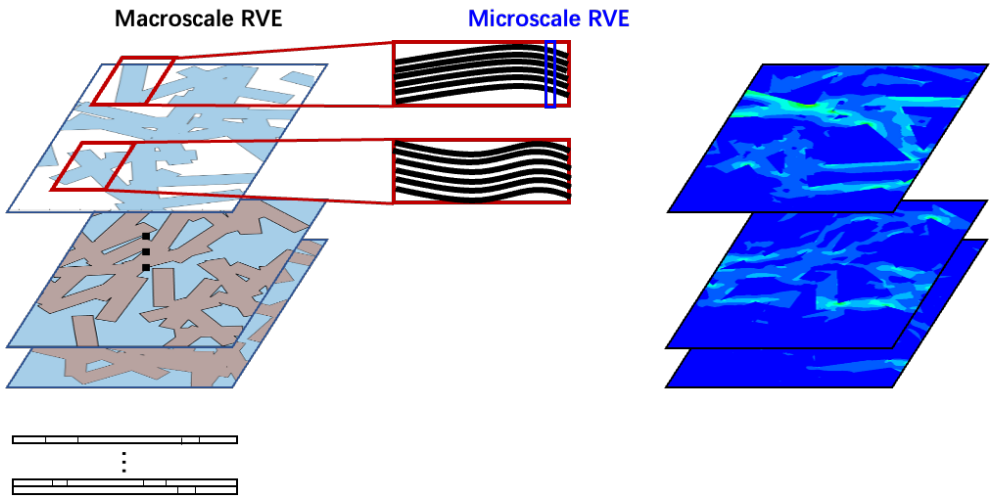

Figure 46. Layered SMC composites

In Figure 46, the layered structure of SMC (Sheet Molding Compound) composites is depicted, representing a realistic depiction of the manufacturing process involved in molding these composites. Each layer of the SMC composite consists of multiple SMC chips, with each chip containing randomly generated orientations. Furthermore, within each SMC chip, randomly wavy fibers are incorporated, reflecting the inherent variability of the composite material.

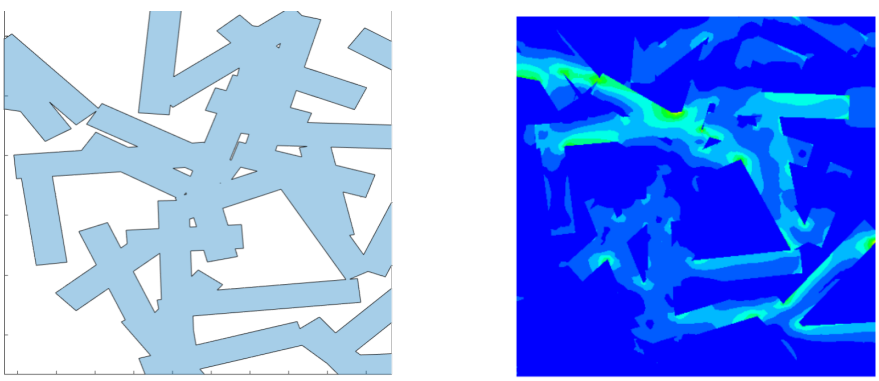

(a) (b)

Figure 47. (a) SMC chip distribution (b) Stress contour of macroscale SMC composites

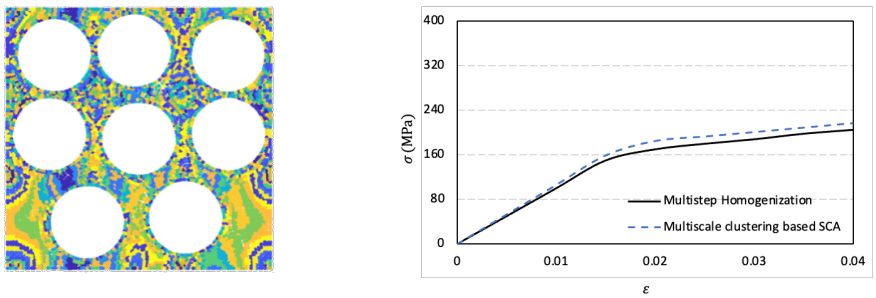

(a) (b)

Figure 48. (a) Cluster distribution of microscale model (b) Comparison of multi-step homogenization and multiscale clustering-based SCA

The comparison between two homogenization methods presented in Chapter 5 is depicted in Figure 48(b), demonstrating their validation and accuracy. It is worth noting that Lippmann-Schwinger homogenization is a multiscale computational model, whereas Mori-Tanaka homogenization is a multiscale numerical model. The material properties utilized in the two homogenization models are obtained from Table 2. The random orientation distribution of SMC chips in the composite and the stress contour of the macroscale SMC model are depicted in Figure 47. On the other hand, Figure 48(a) showcases the fiber-reinforced model with a 64-cluster distribution in the microscale model. Despite their different approaches, both methods exhibit similar trends in terms of elastic and plastic behavior.

Chapter 5. Conclusions

In conclusion, this thesis has presented computational and analytical homogenization approaches for SMC composites, specifically considering the presence of random wavy fibers. Comparing with existing research, the computational homogenization method for SMC composites has been well developed, taking into account the reconstruction of randomly oriented and overlapping SMC chips. However, the computational cost remains high due to the multiscale simulation and detailed structure modeling involved. To address this challenge, the proposed cluster-based method significantly improves computational efficiency while maintaining accuracy.

On the other hand, the proposed analytical homogenization method for SMC composites offers a detailed description of the random wavy fibers and overlapping issues, employing an improved multistep Mori-Tanaka method. This approach shows promising accuracy in capturing the behavior of SMC composites.

Nevertheless, further improvements are still required for the microscale model's representative volume element (RVE). This includes considering the randomness in the cross-section of fibers and their distribution. Additionally, compression and shear loadings are areas that warrant further testing and investigation.

Overall, this thesis contributes to the advancement of homogenization techniques for SMC composites, demonstrating the importance of considering random wavy fibers and providing avenues for future research and refinement in capturing the intricate behavior of these materials.

Bibliography

1. Collins, P.G. and P. Avouris, *Nanotubes for electronics.* Scientific american, 2000. **283**(6): p. 62-69.

2. Iijima, S., *Helical microtubules of graphitic carbon.* nature, 1991. **354**(6348): p. 56-58.

3. Mittal, G., et al., *A review on carbon nanotubes and graphene as fillers in reinforced polymer nanocomposites.* Journal of Industrial and Engineering Chemistry, 2015. **21**: p. 11-25.

4. Liew, K., Z. Lei, and L. Zhang, *Mechanical analysis of functionally graded carbon nanotube reinforced composites: a review.* Composite Structures, 2015. **120**: p. 90-97.

5. Gohardani, O., M.C. Elola, and C. Elizetxea, *Potential and prospective implementation of carbon nanotubes on next generation aircraft and space vehicles: A review of current and expected applications in aerospace sciences.* Progress in Aerospace Sciences, 2014. **70**: p. 42-68.

6. Rafiee, R. and R.M. Moghadam, *On the modeling of carbon nanotubes: a critical review.* Composites Part B: Engineering, 2014. **56**: p. 435-449.

7. De Volder, M.F., et al., *Carbon nanotubes: present and future commercial applications.* science, 2013. **339**(6119): p. 535-539.

8. Khan, S.U., J.R. Pothnis, and J.-K. Kim, *Effects of carbon nanotube alignment on electrical and mechanical properties of epoxy nanocomposites.* Composites Part A: Applied Science and Manufacturing, 2013. **49**: p. 26-34.

9. Zare, Y. and H. Garmabi, *Attempts to simulate the modulus of polymer/carbon nanotube nanocomposites and future trends.* Polymer Reviews, 2014. **54**(3): p. 377-400.

10. Shokrieh, M. and R. Rafiee, *A review of the mechanical properties of isolated carbon nanotubes and carbon nanotube composites.* Mechanics of composite materials, 2010. **46**: p. 155-172.

11. Hammerand, D.C., G.D. Seidel, and D.C. Lagoudas, *Computational micromechanics of clustering and interphase effects in carbon nanotube composites.* Mechanics of Advanced Materials and Structures, 2007. **14**(4): p. 277-294.

12. Fisher, F., R. Bradshaw, and L. Brinson, *Effects of nanotube waviness on the modulus of nanotube-reinforced polymers.* Applied Physics Letters, 2002. **80**(24): p. 4647-4649.

13. Bradshaw, R., F. Fisher, and L. Brinson, *Fiber waviness in nanotube-reinforced polymer composites—II: modeling via numerical approximation of the dilute strain concentration tensor.* Composites Science and Technology, 2003. **63**(11): p. 1705-1722.

14. Shao, L., et al., *Prediction of effective moduli of carbon nanotube-reinforced composites with waviness and debonding.* Composite structures, 2009. **87**(3): p. 274-281.

15. Anumandla, V. and R.F. Gibson, *A comprehensive closed form micromechanics model for estimating the elastic modulus of nanotube-reinforced composites.* Composites Part A: Applied Science and Manufacturing, 2006. **37**(12): p. 2178-2185.

16. Seidel, G.D. and D.C. Lagoudas, *Micromechanical analysis of the effective elastic properties of carbon nanotube reinforced composites.* Mechanics of Materials, 2006. **38**(8-10): p. 884-907.

17. Odegard, G., et al., *Constitutive modeling of nanotube-reinforced polymer composites.* Composites science and technology, 2003. **63**(11): p. 1671-1687.

18. Mallick, P.K., *Fiber-reinforced composites: materials, manufacturing, and design*. 2007: CRC press.

19. Vassilopoulos, A.P. and T. Keller, *Fatigue of fiber-reinforced composites*. 2011: Springer Science & Business Media.

20. Ashbee, K.H., *Fundamental principles of fiber reinforced composites*. 1993: CRC Press.

21. Zhang, M. and J.P. Matinlinna, *E-glass fiber reinforced composites in dental applications.* Silicon, 2012. **4**: p. 73-78.

22. Freilich, M.A., et al., *Development and clinical applications of a light-polymerized fiber-reinforced composite.* The Journal of prosthetic dentistry, 1998. **80**(3): p. 311-318.

23. Jendli, Z., et al., *Micromechanical analysis of strain rate effect on damage evolution in sheet molding compound composites.* Composites Part A: Applied Science and Manufacturing, 2004. **35**(7-8): p. 779-785.

24. Fette, M., Hentschel, M., Santafe, J.G., Wille, T., Büttemeyer, H. and Schiebel, P., *New methods for computing and developing hybrid sheet molding compound structures for aviation industry.* Procedia CIRP, 2017. **66**: p. 45-50.

25. Wu, Y., Xia, C., Cai, L., Garcia, A.C. and Shi, S.Q., *Development of natural fiber-reinforced composite with comparable mechanical properties and reduced energy consumption and environmental impacts for replacing automotive glass-fiber sheet molding compound.* J. Clean. Prod., 2018. **184**: p. 92-100.

26. Okabe, T., Motani, T., Nishikawa, M. and Hashimoto, M., *Numerical simulation of microscopic damage and strength of fiber-reinforced plastic composites.* Adv. Compos. Mater., 2012. **21**(2): p. 147-163.

27. Liu, H., Zeng, D., Li, Y. and Jiang, L, *Development of RVE-embedded solid elements model for*

predicting effective elastic constants of discontinuous fiber reinforced composites. Mech. Mater., 2016. **93**: p. 109-123.

28. Goris, S., Back, T., Yanev, A., Brands, D., Drummer, D. and Osswald, T.A., *A novel fiber length measurement technique for*

discontinuous fiber-reinforced composites: A comparative study with existing

methods. Polym. Compos., 2018. **39**(11): p. 4058-4070.

29. Martulli, L.M., Creemers, T., Schöberl, E., Hale, N., Kerschbaum, M., Lomov, S.V. and Swolfs, Y, *A thick-walled sheet moulding compound automotive component: Manufacturing and performance.* Compos. Part A Appl. Sci. Manuf., 2020. **128**: p. 15688.

30. Trauth, A., Pinter, P. and Weidenmann, K.A., *Investigation of quasi-static and dynamic material properties of a structural sheet molding compound combined with acoustic emission damage analysis.* J. Compos. Sci., 2017. **1**(2): p. 18.

31. Zhu, F.Y., Jeong, S., Lim, H.J. and Yun, G.J., *Probabilistic multiscale modeling of 3D randomly oriented and aligned wavy CNT nanocomposites and RVE size determination.* Compos. Struct., 2018. **195**: p. 265-275.

32. Jeong, S., Zhu, F., Lim, H., Kim, Y. and Yun, G.J., *3D stochastic computational homogenization model for carbon fiber reinforced CNT/epoxy composites with spatially random properties.* Compos. Struct., 2019. **207**: p. 858-870.

33. Lim, H.J., Choi, H., Lee, M.J. and Yun, G.J., *An efficient multi-scale model for needle-punched Cf/SiCm composite materials with experimental validation.* Compos. Part B Eng., 2021. **217**: p. 108890.

34. Jiang, B., Liu, C., Zhang, C., Wang, B. and Wang, Z., *The effect of non-symmetric distribution of fiber orientation and aspect ratio on elastic properties of composites.* Compos. Part B Eng., 2007. **38**(1): p. 24-34.

35. Li, Y., Chen, Z., Xu, H., Dahl, J., Zeng, D., Mirdamadi, M. and Su, X., *Modeling and simulation of compression molding process for Sheet Molding Compound (SMC) of chopped carbon fiber composites.* SAE Int. J. Mater. Manuf., 2017. **10**(2): p. 130-137.

36. Chen, Z., Huang, T., Shao, Y., Li, Y., Xu, H., Avery, K., Zeng, D., Chen, W. and Su, X, *Multiscale finite element modeling of sheet molding compound (SMC) composite structure based on stochastic mesostructure reconstruction.* Compos. Struct., 2018. **188**: p. 25-38.

37. Sun, Q., et al., *An Integrated Computational Materials Engineering Framework to Analyze the Failure Behaviors of Carbon Fiber Reinforced Polymer Composites for Lightweight Vehicle Applications.* Compos Sci Technol, 2021. **202**: p. 108560.

38. Bostanabad, R., et al., *Uncertainty quantification in multiscale simulation of woven fiber composites.* Computer Methods in Applied Mechanics and Engineering, 2018. **338**: p. 506-532.

39. He, C., et al., *From microscale to mesoscale: The non-linear behavior prediction of 3D braided composites based on the SCA2 concurrent multiscale simulation.* Composites Science and Technology, 2021. **213**: p. 108947.

40. Elmasry, A., et al., *A comparative review of multiscale models for effective properties of nano-and micro-composites.* Progress in Materials Science, 2022: p. 101022.

41. Bostanabad, R., et al., *Multiscale simulation of fiber composites with spatially varying uncertainties*, in *Uncertainty Quantification in Multiscale Materials Modeling*. 2020, Elsevier. p. 355-384.

42. Popat, K. and R.W. Picard, *Cluster-based probability model and its application to image and texture processing.* IEEE Transactions on Image Processing, 1997. **6**(2): p. 268-284.

43. Abdullah, D., et al., *The application of K-means clustering for province clustering in Indonesia of the risk of the COVID-19 pandemic based on COVID-19 data.* Quality & Quantity, 2022. **56**(3): p. 1283-1291.

44. Sun, C.-T. and R.S. Vaidya, *Prediction of composite properties from a representative volume element.* Composites science and Technology, 1996. **56**(2): p. 171-179.

45. Xia, Z., Y. Zhang, and F. Ellyin, *A unified periodical boundary conditions for representative volume elements of composites and applications.* International journal of solids and structures, 2003. **40**(8): p. 1907-1921.

46. Mahdi, M. and L. Zhang, *A finite element model for the orthogonal cutting of fiber-reinforced composite materials.* Journal of materials processing technology, 2001. **113**(1-3): p. 373-377.

47. Desai, A. and M.A. Haque, *Mechanics of the interface for carbon nanotube-polymer composites.* Thin-walled structures, 2005. **43**(11): p. 1787-1803.

48. Affdl, J.H. and J. Kardos, *The Halpin-Tsai equations: a review.* Polymer Engineering & Science, 1976. **16**(5): p. 344-352.

49. Coleman, J.N., et al., *Small but strong: a review of the mechanical properties of carbon nanotube-polymer composites.* Carbon, 2006. **44**(9): p. 1624-1652.

50. Thostenson, E.T. and T.-W. Chou, *On the elastic properties of carbon nanotube-based composites: modelling and characterization.* Journal of Physics D: Applied Physics, 2003. **36**(5): p. 573.

51. Hopkins, D.A. and C.C. Chamis, *A unique set of micromechanics equations for high temperature metal matrix composites.* Testing technology of metal matrix composites, ASTM STP, 1988. **964**: p. 159-176.

52. Bunsell, A.R., S. Joannès, and A. Thionnet, *Fundamentals of fibre reinforced composite materials*. 2021: CRC Press.

53. Caruso, J.J. and C.C. Chamis, *Assessment of simplified composite micromechanics using three-dimensional finite-element analysis.* J. Compos. Technol. Res.;(United States), 1986. **8**.

54. Huang, J. and D. Rodrigue, *Equivalent continuum models of carbon nanotube reinforced polypropylene composites.* Materials & Design, 2013. **50**: p. 936-945.

55. Finegan, I.C., *Analytical and experimental study of improvement of damping at the micromechanical level in polymer composite materials by the use of special fiber coatings*. 1997: Wayne State University.

56. Duong, H.M., et al., *Computational modeling of the thermal conductivity of single-walled carbon nanotube–polymer composites.* Nanotechnology, 2008. **19**(6): p. 065702.

57. Shokrieh, M.M. and R. Rafiee, *Stochastic multi-scale modeling of CNT/polymer composites.* Computational Materials Science, 2010. **50**(2): p. 437-446.

58. Hashin, Z. and S. Shtrikman, *A variational approach to the theory of the elastic behaviour of multiphase materials.* Journal of the Mechanics and Physics of Solids, 1963. **11**(2): p. 127-140.

59. Moulinec, H. and P. Suquet, *A fast numerical method for computing the linear and nonlinear mechanical properties of composites.* Comptes rendus de l'Académie des sciences. Série II. Mécanique, physique, chimie, astronomie, 1994.

60. Brisard, S. and L. Dormieux, *Combining Galerkin approximation techniques with the principle of Hashin and Shtrikman to derive a new FFT-based numerical method for the homogenization of composites.* Computer Methods in Applied Mechanics and Engineering, 2012. **217**: p. 197-212.

61. Schneider, M., *Lippmann-Schwinger solvers for the computational homogenization of materials with pores.* International Journal for Numerical Methods in Engineering, 2020. **121**(22): p. 5017-5041.

62. Ma, R. and T.J. Truster, *FFT-based homogenization of hypoelastic plasticity at finite strains.* Computer Methods in Applied Mechanics and Engineering, 2019. **349**: p. 499-521.

63. Brisard, S., *Reconstructing displacements from the solution to the periodic Lippmann–Schwinger equation discretized on a uniform grid.* International Journal for Numerical Methods in Engineering, 2017. **109**(4): p. 459-486.

64. Dorn, C. and M. Schneider, *Lippmann-Schwinger solvers for the explicit jump discretization for thermal computational homogenization problems.* International Journal for Numerical Methods in Engineering, 2019. **118**(11): p. 631-653.

65. Huang, O., et al., *An introduction to kernel and operator learning methods for homogenization by self-consistent clustering analysis.* Computational Mechanics, 2023: p. 1-25.

66. Zaslavsky, M., et al., *Hybrid finite-difference integral equation solver for 3D frequency domain anisotropic electromagnetic problems.* Geophysics, 2011. **76**(2): p. F123-F137.

67. Liu, Z.-C., et al. *Electromagnetic retrieval of missing fibers in periodic fibered laminates via sparsity concepts*. in *2016 24th European Signal Processing Conference (EUSIPCO)*. 2016. IEEE.

68. Dederichs, P.H. and R. Zeller, *Variational treatment of the elastic constants of disordered materials.* Zeitschrift für Physik A Hadrons and nuclei, 1973. **259**(2): p. 103-116.

69. Fassi-Fehri, O., *Le problème de la paire d'inclusions plastiques et hétérogènes dans une matrice anisotrope: application à l'étude du comportement des matériaux composites et de la plasticité*. 1985, Université Paul Verlaine-Metz.

70. MacQueen, J. *Classification and analysis of multivariate observations*. in *5th Berkeley Symp. Math. Statist. Probability*. 1967. University of California Los Angeles LA USA.

71. Liu, Z., M. Bessa, and W.K. Liu, *Self-consistent clustering analysis: an efficient multi-scale scheme for inelastic heterogeneous materials.* Computer Methods in Applied Mechanics and Engineering, 2016. **306**: p. 319-341.

72. Mori, T. and K. Tanaka, *Average stress in matrix and average elastic energy of materials with misfitting inclusions.* Acta metallurgica, 1973. **21**(5): p. 571-574.

73. Qiu, Y. and G. Weng, *On the application of Mori-Tanaka's theory involving transversely isotropic spheroidal inclusions.* International Journal of Engineering Science, 1990. **28**(11): p. 1121-1137.

74. Pettermann, H., et al., *A thermo-elasto-plastic constitutive law for inhomogeneous materials based on an incremental Mori-Tanaka approach.* Computers & Structures, 1999. **71**(2): p. 197-214.

75. Pettermann, H.E., et al., *An incremental Mori-Tanaka homogenization scheme for finite strain thermoelastoplasticity of MMCs.* Materials, 2010. **3**(1): p. 434-451.

76. Koyama, S., et al., *A modification of the Mori-Tanaka estimate of average elastoplastic behavior of composites and polycrystals with interfacial debonding.* Mechanics of materials, 2011. **43**(10): p. 538-555.

77. Czarnota, C., et al., *Modeling of the cyclic behavior of elastic-viscoplastic composites by the additive tangent Mori-Tanaka approach and validation by finite element calculations.* International Journal of Solids and Structures, 2015. **56**: p. 96-117.

78. Sadowski, P., K. Kowalczyk-Gajewska, and S. Stupkiewicz, *Response discontinuities in the solution of the incremental Mori-Tanaka scheme for elasto-plastic composites.* Arch. Mech, 2017. **69**(1): p. 3-27.

79. Sadowski, P., K. Kowalczyk-Gajewska, and S. Stupkiewicz, *Consistent treatment and automation of the incremental Mori-Tanaka scheme for elasto-plastic composites.* Computational Mechanics, 2017. **60**: p. 493-511.

80. Tan, H., et al., *The Mori-Tanaka method for composite materials with nonlinear interface debonding.* International Journal of Plasticity, 2005. **21**(10): p. 1890-1918.

81. Tan, H., et al., *Constitutive behaviors of composites with interface debonding: the extended Mori-Tanaka method for uniaxial tension.* International Journal of Fracture, 2007. **146**: p. 139-148.
82. Mercier, S. and A. Molinari, *Homogenization of elastic–viscoplastic heterogeneous materials: Self-consistent and Mori-Tanaka schemes.* International Journal of Plasticity, 2009. **25**(6): p. 1024-1048.
83. Böhm, H.J. and S. Nogales, *Mori–Tanaka models for the thermal conductivity of composites with interfacial resistance and particle size distributions.* Composites Science and Technology, 2008. **68**(5): p. 1181-1187.
84. Vorel, J. and M. Sejnoha, *Evaluation of homogenized thermal conductivities of imperfect carbon-carbon textile composites using the Mori-Tanaka method.* arXiv preprint arXiv:0809.5162, 2008.
85. Kamarian, S., M. Shakeri, and M. Yas, *Natural frequency analysis and optimal design of CNT/fiber/polymer hybrid composites plates using mori-tanaka approach, GDQ technique, and firefly algorithm.* Polymer Composites, 2018. **39**(5): p. 1433-1446.
86. García-Macías, E., et al., *Eshelby-Mori-Tanaka approach for post-buckling analysis of axially compressed functionally graded CNT/polymer composite cylindrical panels.* Composites Part B: Engineering, 2017. **128**: p. 208-224.
87. Heshmati, M. and M. Yas, *Free vibration analysis of functionally graded CNT-reinforced nanocomposite beam using Eshelby-Mori-Tanaka approach.* Journal of Mechanical Science and Technology, 2013. **27**: p. 3403-3408.
88. Xin, L., et al., *An approximate analytical solution based on the Mori–Tanaka method for functionally graded thick-walled tube subjected to internal pressure.* Composite Structures, 2016. **135**: p. 74-82.
89. Shen, H.-S. and Z.-X. Wang, *Assessment of Voigt and Mori–Tanaka models for vibration analysis of functionally graded plates.* Composite Structures, 2012. **94**(7): p. 2197-2208.
90. Imani, S.M., et al., *The modified Mori-Tanaka scheme for the prediction of the effective elastic properties of highly porous ceramics.* Ceramics International, 2018. **44**(14): p. 16489-16497.
91. Qu, J., *The effect of slightly weakened interfaces on the overall elastic properties of composite materials.* Mechanics of Materials, 1993. **14**(4): p. 269-281.
92. Barai, P. and G.J. Weng, *A theory of plasticity for carbon nanotube reinforced composites.* International Journal of Plasticity, 2011. **27**(4): p. 539-559.
93. Pan, Y., et al., *Interface effects on the viscoelastic characteristics of carbon nanotube polymer matrix composites.* Mechanics of Materials, 2013. **58**: p. 1-11.
94. Shokrieh, M.M., R. Ghajar, and A.R. Shajari, *The effect of time-dependent slightly weakened interface on the viscoelastic*

properties of CNT/polymer nanocomposites. Composite Structures, 2016. **146**: p. 122-131.

95. Yang, S., et al., *Nonlinear multiscale modeling approach to characterize elastoplastic behavior of CNT/polymer nanocomposites considering the interphase and interfacial imperfection.* International Journal of Plasticity, 2013. **41**: p. 124-146.

96. Lee, S. and S. Ryu, *Theoretical study of the effective modulus of a composite considering the orientation distribution of the fillers and the interfacial damage.* European Journal of Mechanics-A/Solids, 2018. **72**: p. 79-87.

97. Tsai, C.-h., et al., *The effect of inclusion waviness and waviness distribution on elastic properties of fiber-reinforced composites.* Composites Part B: Engineering, 2011. **42**(1): p. 62-70.

98. Vieville, P., A. Bonnet, and P. Lipiński, *Modelling effective properties of composite materials using the inclusion concept. General considerations.* Archives of Mechanics, 2006. **58**(3): p. 207-239.

99. Mura, T., *Micromechanics of defects in solids*. 2013: Springer Science & Business Media.

100. Qu, J., *Eshelby tensor for an elastic inclusion with slightly weakened interface.* 1993.

101. Weng, G., *Some elastic properties of reinforced solids, with special reference to isotropic ones containing spherical inclusions.* International Journal of Engineering Science, 1984. **22**(7): p. 845-856.

102. Hsiao, H.M. and I. Daniel, *Elastic properties of composites with fiber waviness.* Composites Part A: Applied Science and Manufacturing, 1996. **27**(10): p. 931-941.

103. Yanase, K., S. Moriyama, and J. Ju, *Effects of CNT waviness on the effective elastic responses of CNT-reinforced polymer composites.* Acta Mechanica, 2013. **224**(7): p. 1351-1364.

104. Azoti, W., et al., *Mean-field constitutive modeling of elasto-plastic composites using two (2) incremental formulations.* Composite Structures, 2013. **105**: p. 256-262.

105. Görthofer, J., et al., *Computational homogenization of sheet molding compound composites based on high fidelity representative volume elements.* Computational Materials Science, 2020. **174**: p. 109456.

106. Kehrer, L., et al., *Dynamic mechanical analysis of pure and fiber-reinforced thermoset-and thermoplastic-based polymers and free volume-based viscoelastic modeling.* GAMM-Mitteilungen, 2018. **41**(1): p. e201800007.

107. Jēkabsons, N. and S. Fernberg, *Prediction of progressive fracture of SMC by application of bridging laws.* Composites science and technology, 2003. **63**(15): p. 2133-2142.

108. Azoti, W.a.E., A, *Constitutive modelling of ductile damage matrix reinforced by platelets- like particles with imperfect*

interfaces: Application to graphene polymer nanocomposite materials. Compos. Part B Eng., 2017. **113**: p. 53-64.

109. Wan, Y. and J. Takahashi, *Mechanical modeling of CF/PA6 sheet molding compounds with X-ray computed tomography-based internal geometry considerations.* Composites Science and Technology, 2020. **192**: p. 108104.

Abstract in Korean

멀티스케일 유한요소 해석(FEA)은 복합재료의 거동을 모델링하는데 효과적인 방법으로 널리 사용되고 있다. 그러나 멀티스케일 모델은 높은 계산 비용으로 인해 실제 적용 에는 한계가 있다. 본 논문은 정확도를 유지하면서 계산 시간을 줄일 수 있는멀티스케일 클러스터 기반 자기상관 해석 SCA(Self-consistent clustering Analysis)방법을 제안하여 복합재료 해석에 적용하는 것을 목표로 한다. 제안된 모델링 방법을 SMC (Sheet Molding Compound) 복합재료에 적용하여 해석의 효율성과 정확성을 타 해석방법과 비교 검증하였다..

먼저 SMC 복합재료의 효율적인 모델링을 위해 개선된 해석적 균질화 모델과 제안된 클러스터 기반 SCA 모델을 제안하고 비교검증하였다. SMC 복합재료의 복잡한 구조로 인해 전통적인 균질화 모델은 그 거동을 정확하게 모사하는데 한계가 있다. 따라서 개선된 해석적 균질화 모델은 wavy 형상의 섬유, 연성 손상, SMC 칩 방향 및 SMC 칩의 겹침과 같은 요소를 고려하여 Mori-Tanaka 방법을 통합하였다. 반면에 클러스터 기반 SCA 모델은 계산 효율성을 유지하면서 무작위로 wavy 모양의 섬유와 무작위로 방향이 지정된 SMC 칩을 고려하는 수치적 멀티스케일 모델이다. 두 가지 균질화 모델은 엄밀하게 검증되었으며 SMC 복합재료의 거동을 모사하는 데 효과적이고 정확함을 입증하였다. 제시된 SCA 모델과 전통적인 멀티스케일 유한요소해석 모델의 비교를 통해 정확성과 타당성을 유지하면서 계산 시간을 크게 줄인 것을 확인하였다. 섬유와 SMC 칩의 다양한 기하학적 특성이 복합재료의 기계적 특성 예측에 미치는 영향도 분석하였다.